EXPERIMENTAL VALIDATION OF NON-COHESIVE SOIL USING DISCRETE ELEMENT METHOD

A Thesis

Submitted to the Faculty

of

Purdue University

by

Ayan Roy

In Partial Fulfillment of the

Requirements for the Degree

of

Master of Science in Mechanical Engineering

December 2018

Purdue University

Indianapolis, Indiana

THE PURDUE UNIVERSITY GRADUATE SCHOOL
STATEMENT OF COMMITTEE APPROVAL

Dr. Tamer Wasfy
    Department of Mechanical and Energy Engineering
Dr. Andres Tovar
    Department of Mechanical and Energy Engineering
Dr. Hanzim El-Mounayri
    Department of Mechanical and Energy Engineering

Approved by:
    Dr. Sohel Anwar
        Chair of the Graduate Program

ACKNOWLEDGMENTS

This thesis could not have been achievable without the assistance and support of several individuals who in one way or another contributed their valuable help in the preparation and completion of this study.

First of all, I would like to express my special thanks to Dr. Tamer Wasfy for providing this opportunity for me to learn and gain this much experience throughout my study. Without his technical advice and constant support, this work could not be done.

Also, I want to thank my advising committee, Dr. Hazim El-Mounayri and Dr. Andres Tovar for their time and direction during the completion of this thesis.

I also appreciate Mechanical Engineering Department faculty for their instruction and advice through my graduate courses.

I would also like to extend my gratefulness to Valerie Lim Diemer for her kindness in formatting this thesis and assisting me during my graduate studies.

I would like to thank my dear parents and sister for supporting and motivating me through all the stages of my life. I am very proud to have such a nice and warm family.

TABLE OF CONTENTS

LIST OF TABLES

LIST OF FIGURES

ABSTRACT

Roy, Ayan. M.S.M.E., Purdue University, December 2018. Experimental Validation of Non-cohesive Soil Using Discrete Element Method. Major Professor: Tamer Wasfy.

In this thesis, an explicit time integration code which integrates multibody dynamics (MBD) and the discrete element method (DEM) is validated using three previously published steady-state physical experiments for non-cohesive sand-type material, namely: shear-cell for measuring shear stress versus normal stress; penetroplate pressure-sinkage test; and wheel drawbar pull-torque-slip test. The test results are used to calibrate the material properties of the DEM soft soil model and validate the coupled MBD-DEM code. All three tests are important because each test measures specific mechanical characteristics of the soil under various loading conditions. Shear strength of the soil as a function of normal load help to understand shearing of the soil under a vehicle wheel contact patch causing loss of traction. Penetroplate pressure-sinkage test is used to calibrate and validate friction and shear strength characteristics of the soil. Finally the rigid wheel-soil interaction test is used to predict drawbar pull force and wheel torque vs. slip percentage and normal stress for a rigid wheel. Wheel-Soil interaction test is important because it plays the role of ultimate validation of the soil model tuned in the previous two experiments and also shows how the soil model behaves in vehicle mobility applications.

All the aforementioned tests were modeled in the multibody dynamics software using rigid bodies and various joints and actuators. The sand-type material is modeled using discrete cubical particles. A penalty technique is used to impose normal contact constraints (including particle-particle and particle-wall contact). An asperity-based friction model is used to model friction. A Cartesian Eulerian grid contact search algorithm is used to allow fast contact detection between particles.

A recursive bounding box contact search algorithm enabled fast contact detection between the particles and polygonal body surfaces (such as walls, penetrometer, and wheel). The governing equations of motion are solved along with contact constraint equations using a time-accurate explicit solution procedure. The results show very good agreement between the simulation and the experimental measurements. The model is then demonstrated in a full-scale application of high-speed off-road vehicle mobility on the sand-type soil.

1. INTRODUCTION

1.1 Motivation

Off-road locomotion exists since the invention of wheels in 3500 B.C. Off-road equipment and vehicles are widely used in the fields of aerospace, military operations, construction, cross-country transportation, and agriculture. Thought there had been significant growth in technology, development on off-road machineries has been limited to empiricism and trial-error process. Until, the 20^{th} century, development of off-road vehicles did not catch the attention of many engineers and researchers. It is important to predict terrain behavior with respect to soil properties in order to predict the performance of off-road vehicles and equipment in their working environment, such study is called ‘Terramechanics’.

Terramechanics can be divided into: terrain-vehicle mechanics; and terrain-implement mechanics. Terrain-vehicle mechanics deals with tractive performance of a vehicle on an unprepared terrain in order to design the desired following systems:

- Steering system of an off-road Vehicle.
- Suspension System of an off-road vehicle, specifically mitigation of excessive vehicle dynamics.
- Vehicle elements interacting with the terrain directly like tires, wheels, and tracks.
- Driveline and powertrain of an off-road vehicle.
- Vehicle elements to mitigate noise, vibration and harshness (NVH) characteristics of an off-road Vehicle such as cabin, and seats.

Knowledge of terramechanics can guide the automotive engineers in the design decision. Similarly, terrain-implement mechanics can be used to design machinery operating on unprepared terrain.

Analysis of systems with knowledge terramechanics will play a significant role in the development of off-road vehicles and equipment. Therefore, research on soil and predicting soil behavior with respect to its interaction with wheels using multibody techniques and DEM approach will play a key role to develop a methodology to accurately predict 'Mobility and Maneuverability of Vehicles on Soft Soil.'

1.2 Literature Review

1.2.1 Empirical Methods

The problem of accurately modeling the interaction between an off-road machine and the terrain is complex and difficult to solve. To deal with this problem efficiently, empirical approaches have been employed for the study of vehicle mobility. In the empirical method, the vehicle is tested on a range of terrains each of which is identified by field observations and simple measurements [1]. The results of these tests are then empirically correlated and a scale is developed for evaluating terrain trafficability and vehicle mobility. This approach has been employed in the US Army Waterways Experiment Station (WES) [2] and was developed for the very first time during World War II as an aid for military intelligence to evalute terrain trafficability and vehicle mobility capabilities. However, difficulties have been encountered in the evaluation of some tire performance parameters in certain types of sand due to the inability of the empirical approach in providing accurate predictions.

Inspite of the shortcomings, well-developed empirical methods are used in estimating vehicle performance in cases where design features are similar to those that have been tested under matching operating conditions. Although it is uncertain that the same effects would be observed in the evaluation of new design concepts or in the prediction of vehicle performance in new operating environments.

1.2.2 Lumped Parameters Parametric Analysis Methods

We will be looking into the mathematical model approach for the parametric analysis of the performance of off-road vehicles in order to circumvent the limitations of empirical methods mentioned earlier. A pioneering effort in this area was made by Bekker [3] [4] [5]. Computer-aided methods which are based on lumped parameters models for parametric analysis of the performance and design of tracked and off-road wheeled vehicles include: methods for performance and design evaluation of vehicles with flexible tracks (NTVPM), vehicles with long-pitch link tracks (RTVPM), and off-road wheeled vehicles (NWVPM) [1]. These methods are based on the physical nature of vehicle-terrain interaction and terramechanics principles and consider major design features of the vehicle that affect its performance. Also, terrain characteristics, such as pressure-sinkage, shearing characteristics and response to repetitive loading are considered. These computer-aided methods are particularly suited for the evaluation of competing designs, optimization of design parameters, and selection of vehicles for a given mission and environment. They have been successfully used to assist off-road vehicle manufacturers in the development of new products.

Bekker Method

M.G. Bekker, was studying terramechanics during the 1950s and 1960s, and created semi-empirical equations for vehicle performance on soft soils which created the foundation for many terramechanics studies [3] [4] [5]. The original Bekker equations are modified and improved to fit researches being performed now. The Bekker method assumed the wheel-soil interface in a 2 dimensional plane, considereing the wheel to be a simple circle operating on a flat leveled soil plane. Wheel dips into the soil because of the applied normal load and slip s, creating an entry contact angle θ_f and exit contact angle θ_r. Wheel slip ratio, which depends on the angular velocity ω, the linear velocity v_x, and the wheel radius r, is defined by

$$s = (\omega r - v_x)/v_x \tag{1}$$

Along the wheel-soil interface normal stresses σ and tangential stresses τ develop, which can be integrated to find the forces acting on the wheel. The normal force, drawbar force (sum of thrust and resistance forces), anddriving torque is defined by

$$F_{normal} = rb\int_{\theta_r}^{\theta_f} (\sigma cos\theta + \tau sin\theta)\, d\theta \tag{2}$$

$$F_{drawbar} = rb\int_{\theta_r}^{\theta_f} (\tau cos\theta - \sigma sin\theta)\, d\theta \tag{3}$$

$$T_{wheel} = r^2 b\int_{\theta_r}^{\theta_f} \tau d\theta \tag{4}$$

where b is the wheel width.

Normal stress along the interface is assumed to be equivalent to the normal pressure on a flat plate at the same sinkage z, the amount of vertical soil compression. The function to calculate normal stress is defined by

$$\sigma = k\left(\frac{z}{b_{plate}}\right)^n \tag{5}$$

where k and n are pressure-sinkage parameters, which can be determined through plate-sinkage experiments, and b_{plate} is the width of the flat plate. The equation for sinkage has been modified somewhat to account for the bow-like shape of normal stress that occurs along the wheel-soil interface [6] [7]. Sinkage along the interface is split between the front and rear regions, defined by

$$z = \begin{cases} r\,(cos\theta - cos\theta_f) & \theta_m \leq \theta \leq \theta_f \\ r\,(cos\theta_{eq} - cos\theta_f) & \theta_r \leq \theta \leq \theta_m \end{cases} \tag{6}$$

where the location of maximum stress θm and the equivalent front-region contact angle θ_{eq} equal

$$\theta_m = (a_0 + a_1 s)\,\theta_f \tag{7}$$

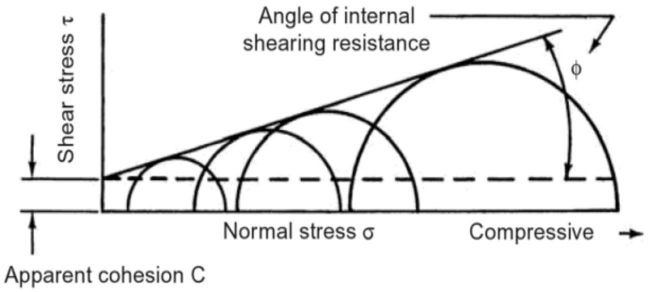

Fig. 1.1. Mohr circle in terramechanics [1].

$$\theta_{eq} = \theta_f - (\theta_f - \theta_m)\,\frac{\theta - \theta_r}{\theta_m - \theta_r} \tag{8}$$

The coefficients a_0 and a_1 are used to empirically adjust the location of maximum stress according to wheel slip s and entry contact angle. The rear contact angle θr was assumed to be zero for the purpose of this study.

$$\begin{gathered}
\tau_{s>=0} = \tau_{res}\left(1 - exp\left(\frac{-|j|}{K}\right)\right) \\
\tau_{s<0} = \begin{cases} -\tau_{res}\left(1 - exp\left(\frac{-|j|}{K}\right)\right) & \theta \geq \theta_m \\ \tau_{res}\left(1 - exp\left(\frac{-|j|}{K}\right)\right) & \theta < \theta_m \end{cases}
\end{gathered} \tag{9}$$

where j is the shear displacement and K is the shear modulus coefficient [8] [9]. The residual shear stress τ_{res} is determined according to the Mohr-Coulomb failure criteria, defined by

$$\tau_{res} = c + \sigma tan\phi \tag{10}$$

where c is the soil cohesion and ϕ is the angle of internal friction, both of which can be determined through soil tests. The shear displacement equation varies based on the slip ratio and the location of the interface [8] [9] given by

$$\begin{gathered}
j_{s>=0} = r\left[(\theta_f - \theta) - (1 - s)\left(sin\theta_f - sin\theta\right)\right] \\
j_{s<0} = \begin{cases} r\,(1 - s)\begin{bmatrix} (\theta_f - \theta)\,\frac{sin\theta_f - \theta_m}{\theta_f - \theta_m} \\ -sin\theta_f + sin\theta \end{bmatrix} & \theta \geq \theta_m \\ r\left[(\theta_m - \theta) - (1 - s)\left(sin\theta_m - sin\theta\right)\right] & \theta < \theta_m \end{cases}
\end{gathered} \tag{11}$$

The Bekker method has several advantages over terramechanics methods, including computation speed. Many of the soil coefficients can be determined through simple soil tests. Some parameters can only be determined if wheel test data is available. The simplicity of the Bekker method creates several limitations. Modeling three-dimensional wheel-soil interaction requires significant modification to the Bekker method to improve numerical accuracy with increased numerical terms.

Dynamic Bekker Method

The Dynamic Bekker method is an enhancement to Bekker method by including multibody dynamics and irregular soil profile which is done considering the wheel as a body with inertia, and discretizing the soil [10]. Therefore the Bekker stress equations are applied to each region of the discretisized soil. The drawbar pull and driving torque are provided by the Langrange multipliers that are calculated by the constrained multibody dynamics problem. A vertical force is given at the wheel center to produce desired normal load. The soil is modeled using a uniformly spaced set of spheres, supported by nonlinear vertical springs. When the soil particles come in contact with the wheel body, the nodes will be displaced creating soil normal pressure.

1.2.3 Computational Methods

Computational methods like the finite element method (FEM) and the discrete (distinct) element method (DEM) have proved beneficial for the analysis of vehicle-terrain interaction due to the recent advancements made in computer technology and the availability of commercial computer codes. They have the potential of providing a tool to examine in detail certain aspects of the mechanics of vehicle terrain interaction [11].

Predictions of tire performance based on these computational methods have been shown to be in qualitative agreement with experimental data on certain types of terrain. For a complex mechanical track system, its interaction with the terrain involves not only the part of the track system in contact with the terrain, but also other factors, such as roadwheel system configuration, suspension characteristics, locations of the sprocket and idler, initial track tension, arrangement of the supporting rollers on the top run of track, etc. To make the analysis responsive to the finite element method, the track usually has to be simplified to a rigid footing with either uniform or trapezoidal form of normal pressure distribution [8] [12]. In many cases, the ratio of the shear stress to normal pressure also needs to be specified.

Discrete Element Method

The discrete element method (DEM) implemented by lumping the soil particles into larger particles, defined by their size, shape, position, velocity, and orientation [9]. A basic DEM model will assume each particle is attached to an adjacent particle with normal spring and damper, tangential spring and damper. These contacting elements are assumed in particle-particle contact (Figure 1.2) and also particle-machine surface contact (Figure 1.3). But it is to be noted that maximum tangential force is limited by the product of the coefficient of friction and the normal force [1]. In Figure 1.2 and Figure 1.3 the spring elements in both the directions cannot sustain tensile forces, because there is no tensile joint in between them as a result of that the effect of cohesion and adhesion is neglected [1]. When Particle collision generates forces and torques using explicit equations. Modeling the soil using this discretized approach allows accounting for significant soil deformation and change in properties due to change in soil structure and non-homogenity [9]. Many researchers have found that when contact is described by only normal and tangential friction forces, more complicated particle shapes like ellipsoids, poly-ellipsoids, polyhedrals can better reproduce soil behavior compared to spheres. Particle collision generates reaction forces which are determind by parameters like length and velocity of particle-particle overlap [13]. In the general DEM [14] [15] inter-particle forces include: normal contact forces (deflection and/or velocity dependent forces which prevent the particles from into penetrating each other), attraction forces, tangential contact forces (friction and viscous forces) and distance dependent forces (gravity, electrostatic and magnetic forces). Particles can be either point particles or rigid body type particles. They can also be spherical, cubical or of any arbitrary shape. References [16] [17] were the first to use DEM to model soils using spherical particles for vehicle mobility applications. In [16] [17] the inter-particle force model included friction and particle stiffness but did not include cohesive (attractive) forces and plasticity. The DEM technique developed in [16] [17] was also extended to non-spherical ellipsoid particles. Cubical rigid body particles were used with a force model that includes normal particle stiffness/damping, tangential viscous and Coulomb friction forces in Wasfy *et al.* [30, 31].

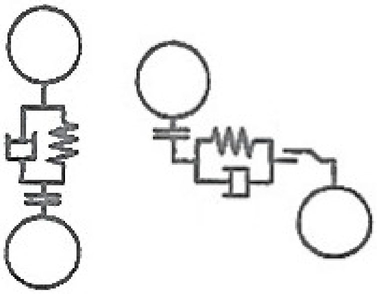

Fig. 1.2. Particle-to-particle normal and tangential contact properties. [1]

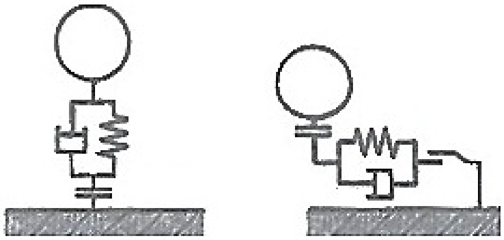

Fig. 1.3. Particle-to-surface Normal and Tangential contact properties. [1]

Finite Element Method

A Lagrangian finite element mesh along with an elastovisco-plastic constitutive material model such as Drucker–Prager model [18] are used for modeling the soil. There are a few disadvantages to this method. Firstly, it cannot capture soil separation/reattachment. Secondly, soil deformation/flow require remeshing and re-interpolating the solution field to the new mesh which is computationally expensive and also the accurcy is compromised. On the other hand, the volume-of-fluid method [19] [20] [21] allows the use of a finite element model while accounting for soil separation/reattachment. Each element has a VOF value between 0 (for empty elements) and 1 (for elements completely filled with fluid/soil). The free surface for each element is reconstructed using piecewise-linear planar segments that are calculated from the VOF value of the element and the VOF values of the neighboring elements. This VOF approach requires the use of an Arbitrary Lagrangian-Eulerian formulation that makes it very difficult to account for soil cohesion and plastic deformation. The finite element method is based on the assumption that the terrain is a continuum which poses limitations in simulating large, discontinuous terrain deformation which often occurs in off-road operations.

1.3 Objectives and Contributions

In this thesis, a three-dimensional DEM model is used along with multibody dynamics model of previously published experiments which include direct shear stress, penetroplate pressure-sinkage test, and rigid-wheel soil interface test to predict various soil characteristics. The DEM model, that is used to model the granular material, supports arbitrarily shaped 3D particles, where each particle is modeled as a rigid body. The particle shape can be represented using: a superquadric surface, a polygonal surface or an assembly of spheres rigidly fixed to the rigid body. The experimental setup is modeled using rigid bodies, joints and actuators. The rigid bodies' rotational equations of motion are written in a body fixed frame with the total rigid body rotation matrix updated each time step using incremental rotations [22]. An asperity-based Coulomb friction model is used to model tangential friction forces [23] between the particles and each other and between the particles and another rigid surface. The friction model along with the accurate representation of the particle shape allows the formation of a stable (static) particle pile and accurate behavior of particles during sliding. A penalty contact technique, with a penalty spring and an asymmetric damper, is used to model normal contact forces. Tangential damping (viscous) forces can also be included in the model. The Eulerian grid space decomposition along with a bounding sphere contact check used in [24] is used in the present model to speed inter-particle contact detection. Contact between rigid bodies (including the particles and rigid components) is detected using a binary tree contact search algorithm which allows fast contact search. A penalty formulation is also used for modeling joint constraints including spherical, revolute, cylindrical and prismatic joints [25]. The equations of motion are integrated using a time accurate explicit predictor-corrector solution procedure.

The main contributions of this thesis are:

- Creating and tuning a non-cohesive DEM soil model by simulating the previously performed and published experiments (direct shear stress test, pressure-sinkage penetrolplate test, rigid wheel soil interface test) in multibody dynamics environment and comparing the results against previously published research work with the same experiments. Each test is a measure of specific mechanical characteristics of the soil under various loading conditions. Shear strength of the soil as a function of normal load help to understand shearing of the soil under a vehicle wheel contact patch causing loss of traction. Penetroplate pressure-sinkage test is used to calibrate and validate friction and shear strength characteristics of the soil. The rigid wheel-soil interaction test is used to predict drawbar pull force and wheel torque vs. slip percentage and normal stress for a rigid wheel.

- The DEM soil model is used in the simulation of a full vehicle MBD model on a sand terrain.

1.4 Tools Used

In this research, the main CAE software tool which was used to create the all the MBD models of the experiments and DEM soil models: DIS (Dynamic Interactions Simulator) [26].DIS is a commercial multibody dynamics code that can be used to simulate mechanical systems which include multiple rigid and flexible components that can come into contact with each other and that are connected using various types of joints. The code also allows adding linear and rotary actuators and the control systems used along with those actuators. The DIS code uses a computationally efficient explicit predictor-corrector time integration method to solve the equations of motion. DIS has been used to predict the dynamic response in many multibody dynamic applications including automotive, aerospace and industrial applications. Further details about the formulation and solution procedure used in the DIS code are provided in next chapter.

1.5 Thesis Organization

This thesis is organized as follows. In Chapter 2, the multibody dynamics formulation and solution procedure used in the DIS code are presented. In Section 2.1, the translational and rotational semi-discrete equations of motion are presented. In Section 2.2, the contact model including the normal force model and tangential asperity friction force model; contact search algorithm; and particle shape representations are presented. In Section 2.3, the penalty algorithm for imposing joint constraints is presented. Linear and rotary actuators models are outlined in Section 2.4. In Section 2.5, the explicit solution procedure is presented. In the following chapters that are Chapter 3, 4 and 5 the experimental and simulation models are explained and the simulation results are compared with previously published experiments for: direct-shear test (Chapter 3), penetroplate test (Chapter 4), rigid-wheel soil interface test (Chapter 5). In Chapter 6, a practical application of the tuned sand-type soil model is shown, with a simulation of a HUMVEE-type vehicle driving over a unpaved track containing the soil model. Finally, concluding remarks and future scope of research are given in Chapter 7.

2. MULTIBODY DYNAMICS FORMULATION

In this chapter, the equations of motion along with the time-integration rule used in the DIS [26] code are outlined. In the subsequent equations, the following conventions are used:

- Indicial notations
- Einstein summation convention for repeated subscript is used
- Upper case subscript indices represent node numbers
- Lower case subscript indices represent vector component number.
- The superscript denotes time.
- A superposed dot denotes a time derivative.

2.1 Equations of Motion

A rigid body is modeled as a finite element node located at the rigid body's center of mass. An algorithm used for generating and integrating the equations of motion for three-dimensional rigid bodies using an explicit finite element [22]. Each node (rigid body) has 3 translational degrees-of-freedom and a rotational matrix is defined with respect to the global inertial.

The translational equations of motion for all nodes are with respect to the global inertial reference frame which is obtained by assembling the individual node equations which can be written as

$$M_K \ddot{x}^t_{ki} = F^t_{s_{Ki}} + F^t_{a_{Ki}} \tag{12}$$

where t is the real time, K is the global node, i is the coordinate number ($i = 1; 2; 3$), M_K is the lumped mass of node K, x is the vector of nodal cartesian coordinates with respect to the global inertial reference frame, $\ddot{x}$ is the vector of nodal accelerations with respect to the global inertial reference frame, F_s is the vector of internal structural forces, and F_a is the vector of externally applied forces, which include surface forces and body forces. For each rigid body (node), a body-fixed material frame is defined. This origin of the body frame is located at the body's center of mass. The mass of the body is concentrated at the center of mass and the inertia of the body is given by the inertia tensor I_{ij} defined with respect to the body frame. The orientation of the body-frame is given by R_k^{t0} which is the rotation matrix relative to the global inertial frame at time t_0. The rotational equations of motions are written for each node with respect to its body-fixed material frames

$$I_{Kij}\ddot{\theta}^t_{Kj} = T^t_{s_{ki}} + T^t_{a_{ki}} - \left(\dot{\theta}^t_{Ki} \times (I_{Kij}\dot{\theta}^t_{Kj})\right)_{Ki} \tag{13}$$

where I_k is the inertia tensor of rigid body K, $\ddot{\theta}_{kj}$and $\dot{\theta}_{kj}$ are the angular acceleration and velocity vectors components for rigid body K relative to its material frame in direction $j(j = 1;\ 2;\ 3), T_{sKi}$ are the components of the vector of internal torque at node K in direction i, and T_{aKi} are the components of the vector of applied torque. The summation convention is used only for the lower case indices i and j. Since, the rigid body rotational equations of motion are written in a body (material) frame, the inertia tensor I_K is constant.

The trapezoidal rule is used as the time integration formula for solving 24 for the global nodal positions x:

$$\begin{aligned} \dot{x}^t_{Kj} &= \dot{x}^{t-\Delta t}_{Kj} + 0.5\Delta t\left(\ddot{x}^t_{Kj} + \ddot{x}^{t-\Delta t}_{Kj}\right) \\ x^t_{Kj} &= x^{t-\Delta t}_{Kj} + 0.5\Delta t\left(\dot{x}^t_{Kj} + \dot{x}^{t-\Delta t}_{Kj}\right) \end{aligned} \tag{14}$$

where Δt is the time step. The trapezoidal rule has been used for the time integration formula for the nodal rotation increments

$$\begin{aligned}\dot{\theta}_{Kj}^{t} &= \dot{\theta}_{Kj}^{t-\Delta t} + 0.5\Delta t\left(\ddot{\theta}_{Kj}^{t} + \ddot{\theta}_{Kj}^{t-\Delta t}\right)\\ \Delta\theta_{Kj}^{t} &= 0.5\Delta t\left(\dot{\theta}_{Kj}^{t} + \dot{\theta}_{Kj}^{t-\Delta t}\right)\end{aligned} \tag{15}$$

where $\mathit{\Delta}\theta_{Kj}$ is the incremental rotation angles around the three body axes for the body K. Thus, the rotational equations of motion are integrated to yield the incremental rotation angles. The rotation matrix of body *K (R_K)* is updated using the rotation matrix corresponding to the incremental rotation angles

$$R_K^t = R_K^{t-\Delta t}\ R\left(\Delta\theta_{Ki}^t\right) \tag{16}$$

where *R(*$\Delta\theta_{Ki}^t$) is the rotation matrix corresponding to the incremental rotation angles from Equation (16). The explicit solution procedure used for solving Equations 12-19 along with constraint equations. The constraint equations are generally algebraic equations, which describe the position or velocity of some of the nodes. They include

- Contact/impact constraints (Section 2.2):

$$f\left(\{x\}\right) \geq 0 \tag{17}$$

- Joint constraints:

$$f\left(\{x\}\right) = 0 \tag{18}$$

- Prescribed motion constraints:

$$f\left(\{x\}, t\right) = 0 \tag{19}$$

2.2 Contact Model

Normal contact constraints between contact point on a rigid body and a surface on another rigid body. The penalty method has been used [22] [27]. The firstly it is important to find the position and velocity of a contact point on a rigid body. The global position x_{Gp} and velocity $\dot{x}_{Gp}$ of a contact point are given by

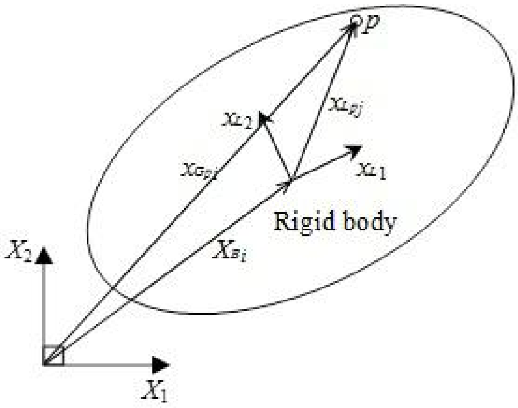

Fig. 2.1. Location of a point on a rigid body with respect to the local body frame (XLP) and the global reference frame (XGP) [28].

$$\begin{aligned} x_{Gp_i} &= X_{B_i} + R_{B_{ij}} x_{Lp_j} \\ \dot{x}_{Gp_i} &= \dot{X}_{B_i} + R_{B_{ij}} (W_{BF} \times x_{Lp})_j \end{aligned} \tag{20}$$

where X_B and $\dot{X}_B$ are the global position and velocity vectors of the rigid body's frame, R_B is the rotation matrix of the rigid body relative to the global reference frame, W_B is the rigid body's angular velocity vector relative to its local frame, and x_{Lp} is the position of the contact point relative to the rigid body's frame. The contact force F_c at each contact point is the sum of the normal contact force (F_n) and tangential friction force (F_t):

$$F_{c_i} = F_{t_i} + F_{n_i} \tag{21}$$

F_c is transferred as a force to the center of the rigid body (the node) using

$$F_i = F_{c_i} \tag{22}$$

$$T_i = (x_{LPi} \times R_{BFji} F_{c_i}) \tag{23}$$

$$x_{LP_j} = R_{BFji} \left(x_{Gp_i} - X_{BF_i} \right) \tag{24}$$

where F_i is the contact force at the CG of the rigid body (center of the body frame), T_i is the contact moment on the rigid body, x_{Lcp} is the position of the contact point relative to the rigid body's frame and x_{Gcp} is the position of the contact point relative to the global reference frame. Similarly, the negative of this force is transferred to the center of the contacting rigid body as a force and moment.

2.2.1 Penalty Normal Contact Model

The penalty technique is used for insuring that particles or rigid bodies do not interpenetrate. A normal reaction force (F_n) is generated when a node penetrates in a contact body whose magnitude is proportional to the penetration distance. The force is given by:

$$|fn| = AK_p d + A \begin{cases} C_p \dot{d} & \dot{d} \geq 0 \\ S_p C_p \dot{d} & \dot{d} < 0 \end{cases} \tag{25}$$

$$\dot{d} = v_{rel_i} \tag{26}$$

$$v_{n_i} = \dot{d}_{n_i} \tag{27}$$

$$V_{t_i} = v_{rel_i} - v_{n_i} \tag{28}$$

where A is the area associated with the contact point, K_p and C_p are the penalty stiffness and damping coefficients per unit area respectively; d is the closest distance between the node and the contact surface as shown in Figure 2.2; $\dot{d}$ is the signed time rate of change of d; S_p is the separation damping factor between 0 and 1 which determines the amount of sticking between the contact node and the contact surface at the node (leaving the body); v_{rel_i} is the relative velocity vector between the contact point and the contact surface; $\overrightarrow{n}$ is the normal to the surface, v_{n_i} is the velocity vector in the direction of $\overrightarrow{n}$, and $\overrightarrow{v}_{t_i}$ is the tangential velocity vector.

2.2.2 Asperity Friction Model

An asperity-spring friction model is used to model contact and joint friction [23]. The model approximates asperity friction where friction forces between two rough

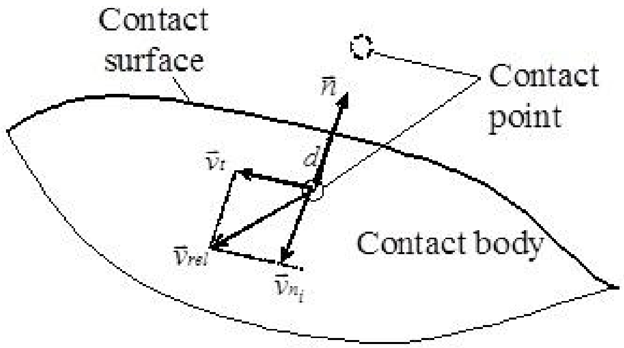

Fig. 2.2. Contact surface and contact node [28]

surfaces in contact arise due to the interaction of the surface asperities Figure 2.3. The tangential friction contact force vector transmitted to the contact body at the contact point. (F_{t_i}) is given by:

$$F_{t_i} = t_i \left| F_t \right| \tag{29}$$

$$t_i = v_{t_i} / \left| \overrightarrow{v_t} \right| \tag{30}$$

where t_i is a unit vector along the tangential contact direction. The asperity friction model is used along with the normal force to calculate the tangential friction force ($|F_t|$) [23]. When two surfaces are in static (stick) contact, the surface asperities act like tangential springs. When a tangential force is applied, the springs elastically deform and pull the surfaces to their original position. If the tangential force is large enough, the surface asperities yield (i.e. the springs break) allowing sliding to occur between the two surfaces. The breakaway force is proportional to the normal contact pressure. In addition, when the two surfaces are sliding past each other, the asperities provide resistance to the motion that is a function of the sliding velocity and acceleration, and the normal contact pressure. Figure 2.3 [29] shows a schematic diagram of the asperity friction model. It is composed of a simple piece-wise linear velocity-dependent approximate Coulomb friction element in parallel with a variable anchor point spring. In order to connect two points on two bodies using an asperity

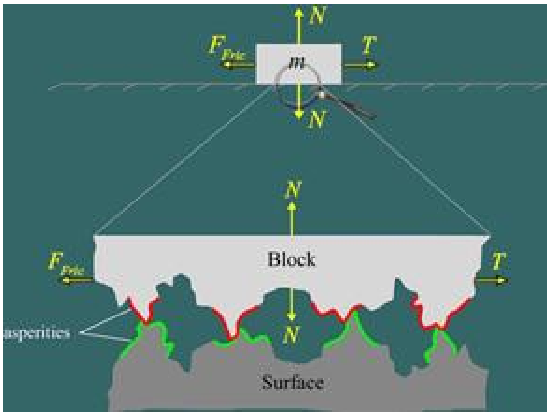

Fig. 2.3. Asperity-based physical interpretation of friction [28]

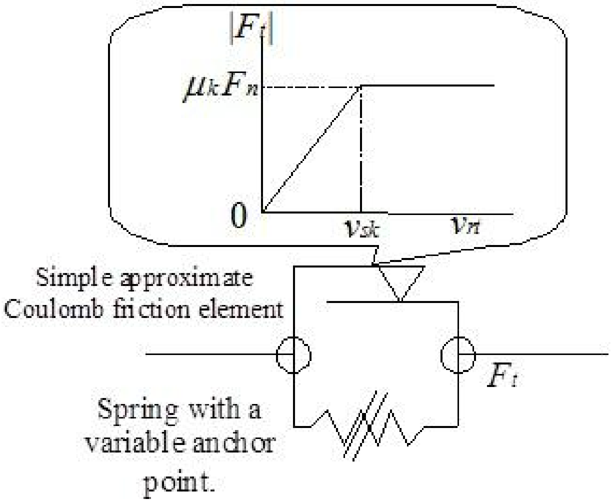

Fig. 2.4. Asperity spring friction model where F_t is the tangential friction force, F_n is the normal force, μ_k is the kinetic friction coefficient, and v_{rt} is the relative tangential velocity between the two points of contact [28]

spring, the model must keep track of which rigid bodies are in contact and of the local position vectors of the asperity spring anchor points on the two contacting bodies. It also must keep track of the corresponding contact points on the two contact bodies.

2.2.3 Inter-Particle Contact Search

Another key component of the DEM is search and detection of inter-particle contacts. In [29] a space decomposition contact search algorithm was developed. This algorithm is implemented to search for particle contact. The steps of the algorithm are as follows:

1. The space where the particles can move is decomposed into a Cartesian Eulerian volume grid of equally sized boxes (Figure 2.5).

2. We loop over all the particles. For each particle, the grid boxes that intersect the particle are found. The minimum and maximum vertical and horizontal grid numbers of a particle can be easily found knowing the position of the center of the particle and the bounding box of the particle. In addition, each grid box has a list of particles that it intersects. Thus, in the same loop for each grid box that intersects the particle we add the particle to the grid box.

3. For each particle the neighbohood particles can come into contact with a particle is generated. This list consists of the particles that intersect the boxes that the particle intersects.

4. For each particle, the distance between the center of the particle and the center of a neighboring particle is calculated. If that distance is larger than the sum of bounding sphere radii of the two particles, then the particles are not in contact. Otherwise, contact point detection is carried out to find the contact point (if any).

5. The algorithm keeps track of the boxes that contain particles and those are initialized to zero particles each time step. This is important since the number of Cartesian boxes is typically much larger than the number of particles [30]. For example in Figure 2.5 :

Particle 6 intersects vertical grids 9 to 11 and horizontal grids 4 to 5.

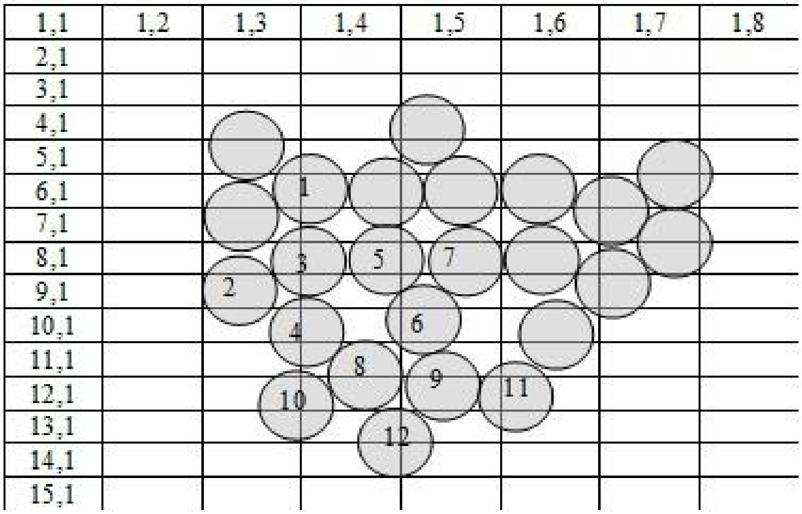

Fig. 2.5. Cartesian grid domain decomposition [30]

Grid (9,4) intersects particles: 3, 4, 5, 6.

Grid (9,5) intersects particles: 5, 6. 7

Grid (10,4) intersects particles: 4, 6

Grid (10, 5) intersects particles: 6

Grid (11, 4) intersects particles: 4, 6, 8, 10

Grid (11,5) intersects particles: 6, 8, 9, 11

Thus, particle 6 neighbors are: particles: 3, 4, 5, 7, 8, 9, 10, 11.

The main algorithm loop runs over the number of particles *N*. Thus, the complexity is *O(N)*. The additional bounding sphere search quickly eliminates most of the neighboring particles thus the particles that the most computationally expensive contact point detection is carried over are the neighboring particles that have a very high likelihood of being in contact with the particle.

2.2.4 Contact Point Search

Superquadric and Spherical Surfaces Contact Search – The detection is performed between contact points on a contact surface of a rigid body, called the master contact surface, and a surface of another rigid body, called the slave contact surface [31]. The slave contact surface can be: a superquadric surface (Figure 2.6) or a collection of bounding spheres (Figure 2.8). A superquadric surface centered at point (0, 0, 0) is defined by:

$$\left(\frac{x_1}{r_1}\right)^{p_1} + \left(\frac{x_2}{r_2}\right)^{p_2} + \left(\frac{x_3}{r_3}\right)^{p_3} = 1 \tag{31}$$

where x_i is the coordinate of a point on the surface, r_i is the radius in direction i, and P_i is the exponent in direction i. If the master contact point coordinates xc_i in the slave contact body frame satisfies the following condition:

$$\left(\frac{x_1}{r_1}\right)^{p_1} + \left(\frac{x_2}{r_2}\right)^{p_2} + \left(\frac{x_3}{r_3}\right)^{p_3} \leq 1 \tag{32}$$

Then the master contact point is inside the contact slave body. Similarly, if the slave contact surface is a collection of spheres (Figure 2.7) then Equation 32 can be used to detect contact if the contact point coordinates xc_i are calculated in the local frame of each sphere on the slave contact body. In the case of a sphere, $p_1 = p_2 = p_3 = 2$, and $r_1 = r_2 = r_3 = r$. In that case Equation 39 becomes:

$$(x_{c_1})^2 + (x_{c_2})^2 + (x_{c_3})^2 \leq r^2 \tag{33}$$

where r is the radius of the sphere.

Fig. 2.6. Particle of cubical shape modeled using superquadric with N = 3 (left) and N = 8 (right) [31]

The sand particle shape model used in the rest of this thesis is the glued sphere model in Figure 2.7. Eight spheres are glued to form a cubical-like particle.

Polygonal Surface Contact Search – This contact model is used to model contact between rigid bodies and the particles. If the slave contact surface is a polygonal

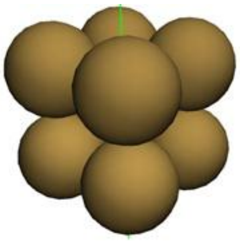

Fig. 2.7. Particle of cubical shape modeled using 8 spheres [31]

surface (see Figures 2.8) binary tree contact search algorithm is employed to detect contact between a contact point of the master surface and the polygons of the slave surface. [31]. Following are the initial steps of the algorithm:

- Each slave polygonal contact surface is divided into 2 blocks of polygons. The bounding box is found for each block and again each block is further divided and bounding boxes found. This recursive division continues until there is only one polygon in a box.

- For each master contact sphere, the radius of the contact sphere is added to the size of the bounding box, then it is checked if the center point of the sphere is inside a bounding box. If it is not, then all the points inside that sphere are concluded to be not in contact with the surface. Otherwise it needs to be determined if the point is inside either box. If it is, then the sub-contact spheres are checked. If a contact point is found to be inside the lowest level bounding box, then a more computationally intensive contact algorithm between a point and a polygon is used to determine the depth of contact and the local position of the contact point on the polygon.

2.3 Joint Constraints

A joint connects two rigid bodies. A joint imposes motion constraints between points on two rigid bodies. All rigid bodies consist of numerous connection points,

Fig. 2.8. Particle of cubical shape modeled using a polygonal surface [31].

these connection points are the points where joints are attached and it does not add DOFs to the system. The position and velocity of a connection point are given by Equations 34 and 35, respectively, where x_{LP} is the position of the connection point relative to the body's frame and x_{GP} and $\dot{x}_{GP}$ are the position and velocity of the connection point relative to the global reference frame.

2.3.1 Revolute Joints

A revolute joint constrains three translational DOFs and two rotational DOFs between two rigid bodies, thus leaving only one rotational DOF free between the bodies. Revolute joints can be modeled by placing two spherical joints along a line. Therefore, the same mathematical methods which are used for the spherical joints can be used to define revolute joints.

2.3.2 Prismatic Joints

A prismatic joint constrains two translational and three rotational DOFs between two rigid bodies and leaves only one translational DOF free Figures 2.14 and 2.15. Prismatic joints can be modeled by placing two cylindrical joints in parallel [30].

Fig. 2.9. Prismatic joint in 2D

2.4 Actuators

2.4.1 Linear Actuator

A linear actuator connects two points on two rigid bodies (Figure 2.16). Using a PD controller, the force F is generated by the actuator is given by:

$$F = K\left(l - l_{des}\right) + c\left(\frac{l_i \dot{l}_i}{l} - i_{des}\right) \tag{34}$$

$$l_i = x^t_{c1_i} - x^t_{c2_i} \tag{35}$$

$$\dot{l}_i = x^t_{c1_i} - x^t_{c2_i} \tag{36}$$

$$l = \sqrt{l_1^2 + l_2^2 + l_3^2} \tag{37}$$

where $x^t_{c1_i}$ is the position of the first point on the first body and $x^t_{c2_i}$ is the position of the second point on the second body, both with respect to the global reference frame; K is the controller proportional gain, c is the controller derivative gain, l_{des} is the desired length of the actuator, l is the current length of the actuator, and is F the actuator force vector [28] [32]. The actuator force is transferred to the rigid bodies center as force and moment using Equations 37 and 38.

2.4.2 Rotational Actuator

A rotational actuator connects three points on two rigid bodies (Figure 2.11). Two of the points are on one rigid body and the remaining point is on the second

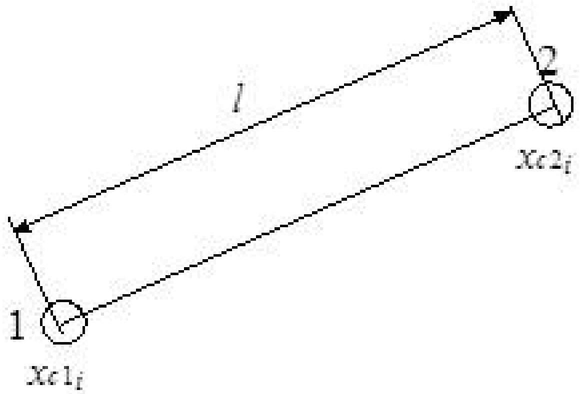

Fig. 2.10. Linear actuator connecting two points [28] [32]

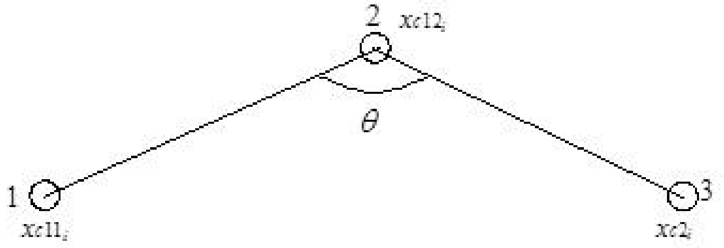

Fig. 2.11. Rotational actuator connecting three points [28] [32]

rigid body. Using a PD controller the torque T generated by the actuator is given by:

$$T = k\left(\theta - \theta_{des}\right) + c\left(\dot{\theta} - \dot{\theta}_{des}\right) \tag{38}$$

where θ is the current angle of the actuator, θ_{des} is the desired angle, k is the proportional gain and c is the derivative gain. The rotary spring forces are transferred to the rigid bodies' center as force and moment using Equations 39, 40.

2.5 Explicit Solution Procedure

The solution fields for modeling multibody systems are defined at the model nodes wherein a rigid body is modeled as one finite element node. The solutions fields are:

- Translational positions
- Translational velocities
- Translational accelerations
- Rotational matrices
- Rotational velocities
- Rotational accelerations

The explicit time integration procedure predicts the time evolution of the above response quantities. The procedure described below achieves near linear speed-up with the number of processors on shared memory parallel computers. The procedure is implemented in the DIS [26] (Dynamic Interactions Simulator) commercial software code and is outlined below:

1. Prepare the run:
    a. Set the initial conditions for the solution fields mentioned above.
    b. Create a list of all the finite elements that includes the master contact surfaces.
    c. Create a list of elements that will run on each processor. This is done using an algorithm which tries to make the computational cost on each processor equal.
    d. Create a list of all the prescribed motion constraints.
    e. Calculate the solid masses for each finite element node by looping through the list of finite elements. Note that the masses are fixed in time.
    f. Loop over all the elements and find the minimum time step for the explicit solution procedure.
2. Loop over the solution time and increment the time by t each step while doing the following:

a. Set the nodal values at the last time step to be equal to the current nodal values for all solution fields.

b. Do 2 iterations (a predictor iteration and a corrector iteration) of the following:

   i. Initialize the nodal forces and moments to zero.

   ii. Perform the particle Contact search algorithm

   iii. Calculate the nodal forces and moments by looping through all the elements while calculating and assembling the element nodal forces. This is the most computationally intensive step. This step is done in parallel by running each list of elements identified in step 1.c on one processor.

   iv. Find the nodal values at the current time step using semi-discrete equations of motion and the trapezoidal time integration rule.

   v. Execute the prescribed motion constraints which set the nodal value(s) to prescribed values.

   vi. Go to beginning of step 2.

3. DIRECT SHEAR TEST

The shear stress-displacement model is intended for the identification of the shear strength specifically the cohesion, angle of friction, shear modulus which will be helpful for prediction of the tractive performance of the vehicles running over unprepared soils. Bekker [3] proposed Eq. (2.15) to describe the shear stress displacement relationship for brittle soils which contains a hump of maximum shear stress [32].

$$\frac{\tau}{\tau_{max}} = \frac{e^{\left(-K_2+\sqrt{K_2^2-1}\right)K_1 j} - e^{\left(-K_2-\sqrt{K_2^2-1}\right)K_1 j}}{e^{\left(-K_2+\sqrt{K_2^2-1}\right)K_1 j_0} - e^{\left(-K_2-\sqrt{K_2^2-1}\right)K_1 j_0}} \tag{39}$$

where,

τ = shear stress

τ_{max} = maximum shear stress

K_1 = empirical parameter in the Bekker shear equation

K_2 = empirical parameter in the Bekker shear equation

j = shear displacement

j_0 = shear displacement at τ_{max}

Janosi and Hanamoto [33] [34] established a modified shear stress-displacement equation based on the Bekker equation. This modified equation is widely used due to the simplicity that only one constant is included.

$$\frac{\tau}{\tau_{max}} = 1 - e^{(-j/K)} \tag{40}$$

where K is the shear deformation modulus

3.1 Experiment and Simulation

The test setup was ASTM International Standard Test Method for Direct Shear Test. [10] The rig consists of three main parts: the carriage and loading box, the motor assembly, and the load cell. The carriage is fitted with a loading box, in which the

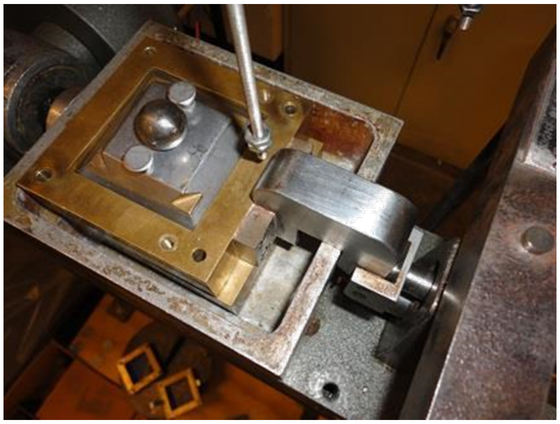

Fig. 3.1. Direct shear stress experimental setup [36]

test material sits. Normal load by putting known weight is given on the loading box. Three different weights have been used in the test and the simulation. Three different soil specimens have been used. Simulation soil model is tuned to co-relate average test results of the three samples. The loading box consists of two halves that are allowed to slide freely, the lower box is given linear displacement in a controlled fashion by a motor in the test rig which is emulated by a linear actuator in the simulation and the displacement and resistive force by the soil is measured. The resistive force exerted tangentially by the soil against the motion of the lower box is measured to create plots of shear stress as a function of shear displacement. The shear stress vs. displacement relationship levels off when the material stops expanding or contracting, and when inter-particle bonds are broken. The shear stress remains constant while the shear displacement increases may be called the critical state, steady state, or residual shear stress [35].

In the simulation it was important to randomize the DEM soil particles to emulate actual condition therefore the soil particle grid box is dropped at a three dimensional angle and the lower box was an attached to a shaker actuator to shake the box and get all the soil particle oriented randomly.

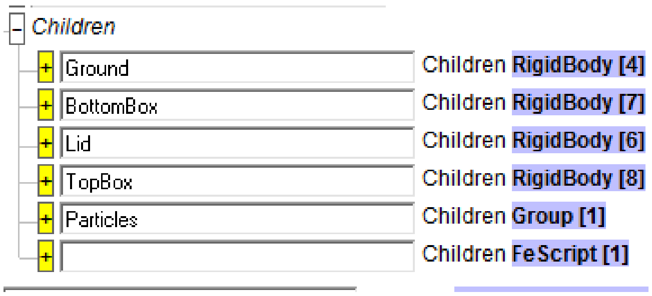

Fig. 3.2. MBD simulation model hierarchy

Table 3.1.
MBD model properties for direct shear stress simulation

Number of rigid bodies	4
Number of prismatic joints	3
Number of linear actuator	3

3.2 Results and Explanation:

The multibody dynamics model of the direct shear stress experiment consist of as shown in Figure 3.2 ground, bottom box, top box, lid and the particles. Table 1 states MBD model properties which consist of 4 rigid bodies, 3 prismatic joints and 3 linear actuators. As shown in Figure 3.3 the linear actuator acting through the prismatic joint of the lid is connected to the top box. The Lid actuator is activated once the particles box grid falls and settles inside the box. The particle box has been given an initial three dimensional angle so that when it falls the particles are well randomized. The total box size used to contain the particles is 60mm x 60mm x 50mm which are the specifications similar to the experiment. The lid is given the normal loads of 6.2 kg, 16.2 kg and 26.2 kg as performed in the experiment. Once the lid reached the particle top surface and stabilized the linear actuator of the top box starts moving the top box linearly relative to the bottom box. The shear force or the resistance force exerted by the particle is measured by a force sensor. All the stages of the simulations are shown in Figure 3.4.

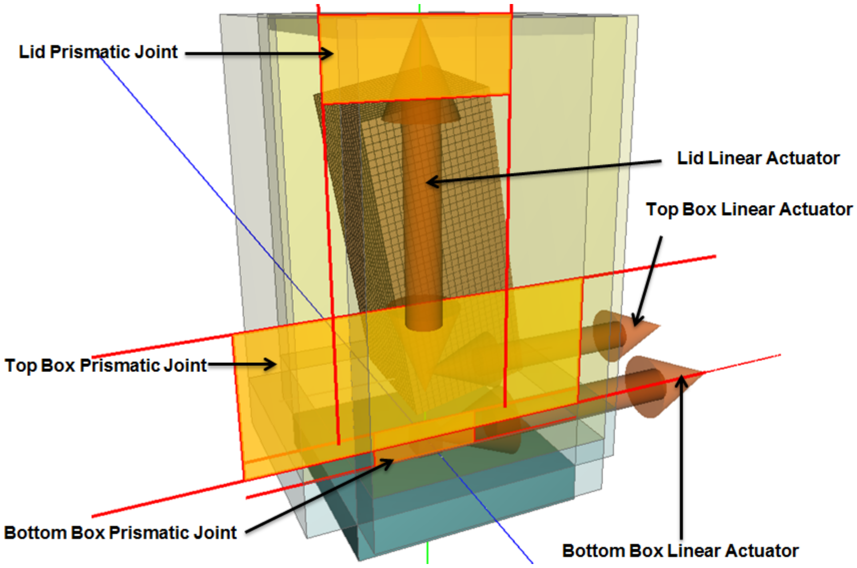

Fig. 3.3. Joints and actuators in the MBD model of direct shear stress test

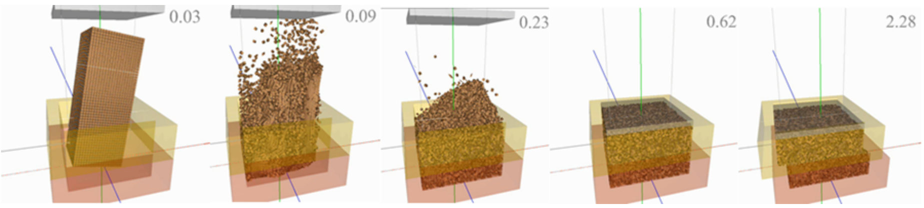

Fig. 3.4. Snapshots of the direct shear stress test experiment

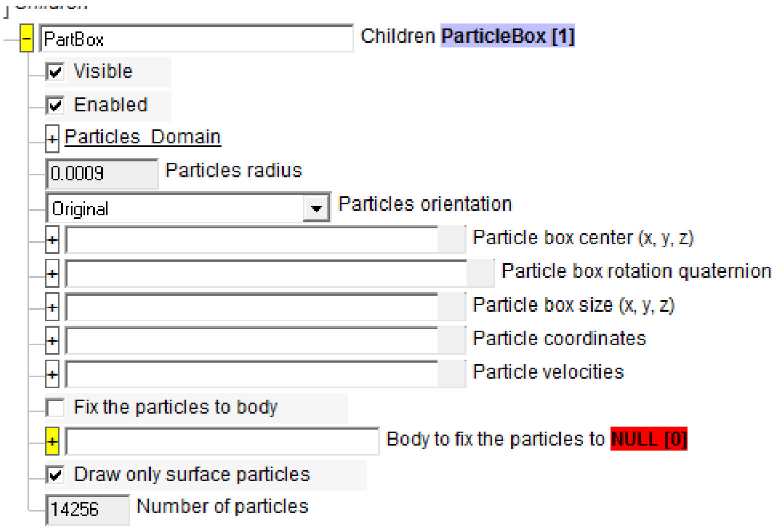

PartBox Children ParticleBox [1]

☑ Visible

☑ Enabled

Particles_Domain

0.0009 Particles radius

Original Particles orientation

Particle box center (x, y, z)

Particle box rotation quaternion

Particle box size (x, y, z)

Particle coordinates

Particle velocities

☐ Fix the particles to body

Body to fix the particles to NULL [0]

☑ Draw only surface particles

14256 Number of particles

Fig. 3.5. DEM particle model inside IVRESS showing number of particles and particle radius

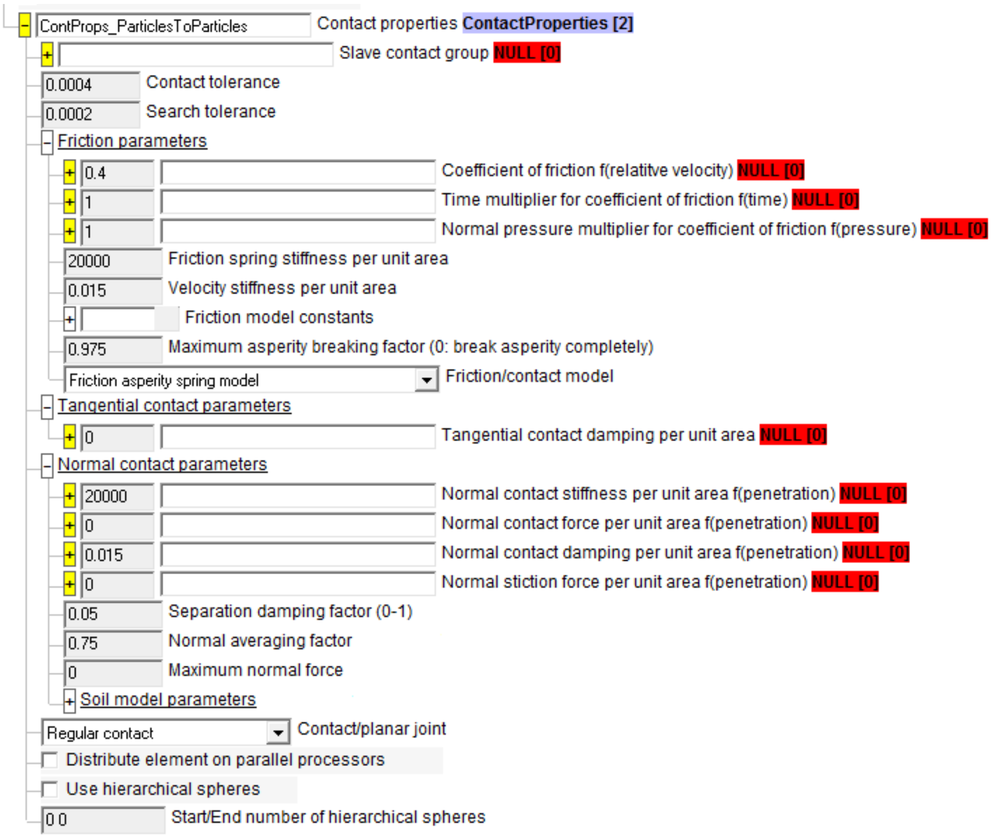

ContProps_ParticlesToParticles Contact properties **ContactProperties [2]**

Slave contact group NULL [0]

0.0004 Contact tolerance

0.0002 Search tolerance

Friction parameters

- 0.4 Coefficient of friction f(relatitve velocity) NULL [0]
- 1 Time multiplier for coefficient of friction f(time) NULL [0]
- 1 Normal pressure multiplier for coefficient of friction f(pressure) NULL [0]
- 20000 Friction spring stiffness per unit area
- 0.015 Velocity stiffness per unit area
- Friction model constants
- 0.975 Maximum asperity breaking factor (0: break asperity completely)
- Friction asperity spring model Friction/contact model

Tangential contact parameters

- 0 Tangential contact damping per unit area NULL [0]

Normal contact parameters

- 20000 Normal contact stiffness per unit area f(penetration) NULL [0]
- 0 Normal contact force per unit area f(penetration) NULL [0]
- 0.015 Normal contact damping per unit area f(penetration) NULL [0]
- 0 Normal stiction force per unit area f(penetration) NULL [0]
- 0.05 Separation damping factor (0-1)
- 0.75 Normal averaging factor
- 0 Maximum normal force
- Soil model parameters

Regular contact Contact/planar joint

☐ Distribute element on parallel processors

☐ Use hierarchical spheres

0 0 Start/End number of hierarchical spheres

Fig. 3.6. IVRESS snapshot showing particle-particle contact properties

Table 3.2.
Particle properties for direct shear stress simulation

Number of particles	14256
Particle radius (m)	0.00207846
Particle shape	Cubical-8 glued spheres
Normal contact stiffness (N)	2000
Normal contact damping (N.sec)	0.015
Separation damping factor	0.05
Coefficient of friction	0.4

As shown in Figure 3.5 total number of particles used is 14256 with particle radius of 0.0009 m. Table 2 shows the particle-particle contact properties which are also shown in the snapshot taken directly from IVRESS in Figure 3.6. The main parameter which was tuned to match the experimental results was the coefficient of friction. The other was chosen to produce rigid cubical-shaped particles.

Direct Shear vs. Displacement Graphs:

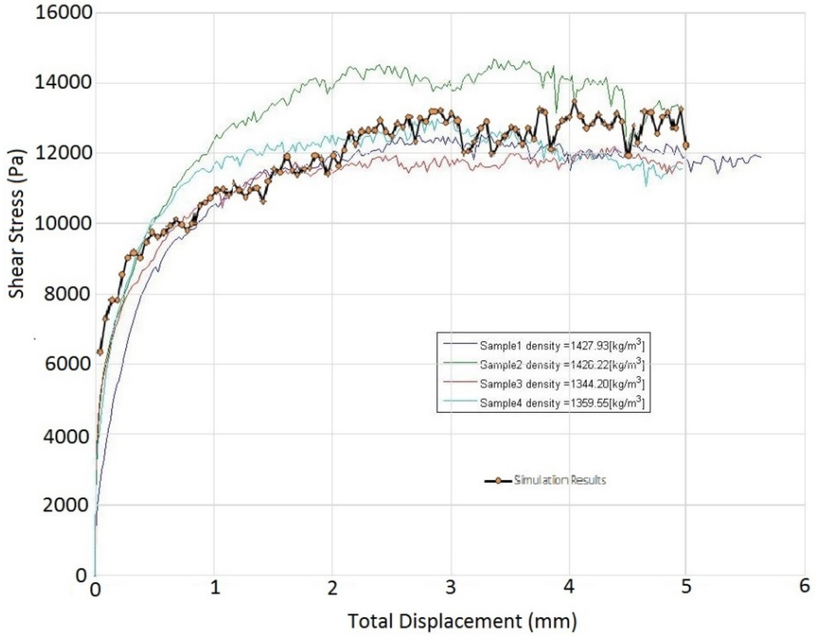

Fig. 3.7. Comparison between simulation and test results with normal load of 16kPa [36]

In Figure 3.7 at load at 16kPa (6.2kg) the DEM soil model's shear stress follows the mean trend of the three soil sample in the experiment.

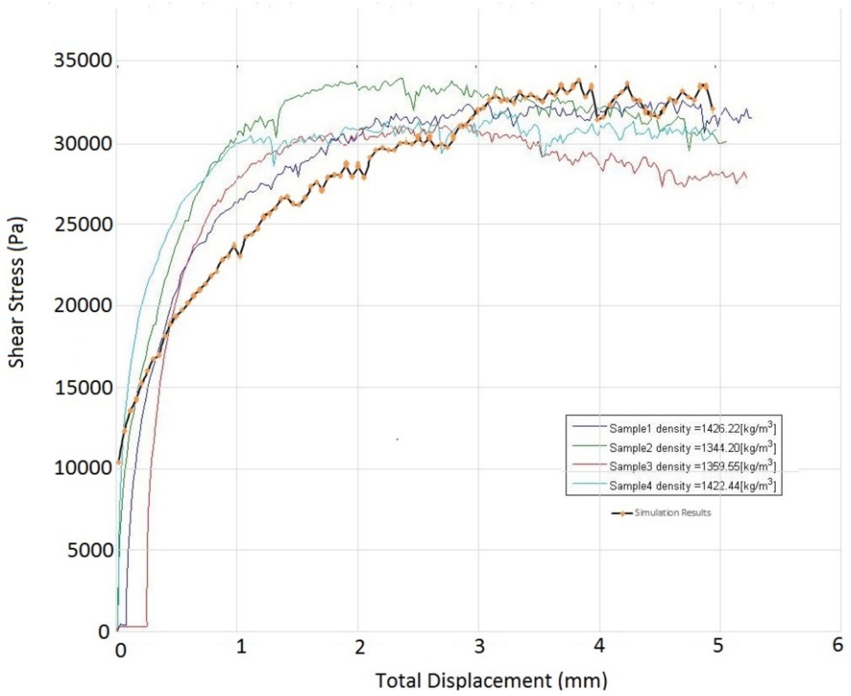

Fig. 3.8. Comparison between simulation and test results with normal load of 44kPa [36]

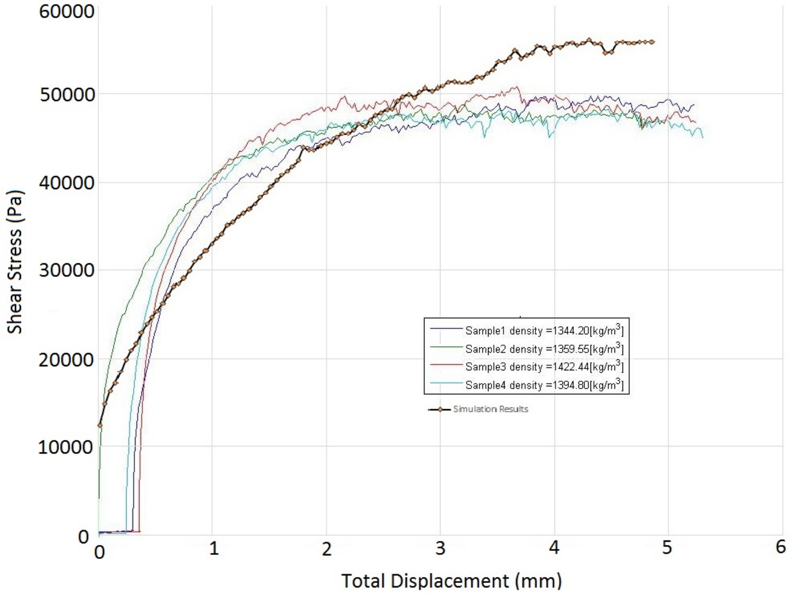

Fig. 3.9. Comparison between simulation and test results with normal load of 71kPa [36]

In Figure 3.8 and Figure 3.9 at load at 44kPa (16.2kg) and 71kpa (26.2kg) the shear stress of DEM soil model has a lower initial slope than the experiment and the stead-state shear stress is slightly higher than the experiment. The slope difference can be due to the different speed shearing and the fact that the physical particles size is much smaller than the size of the DEM particles.

Direct Shear vs. Normal Load Graph:

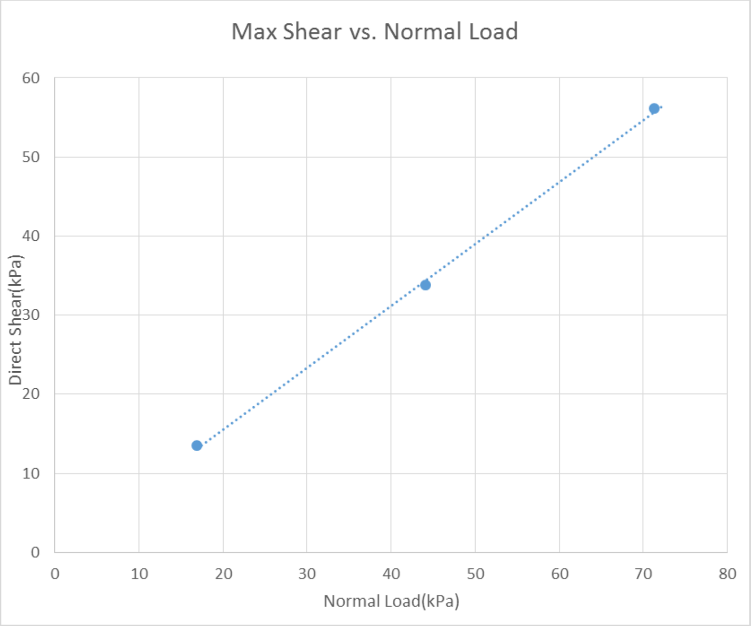

Fig. 3.10. Maximum shear stress plot of all the three simulations with varying normal load

Figure 3.10 confirms the soil is non-cohesive as cohesivity (c) is found to be zero and angle of friction (phi) is 38.043 degrees compared to 34.2 degrees and 43.5 degrees of the low and high density soil sample used in the experiment.

Table 3.3.
Maximum direct shear stress at different normal load

Normal Load(kPa)	Max Shear(kPa)
16.895	13.48302778
44.145	33.79444444
71.395	56.12888889
Phi(deg)	38.043
c	0

4. PRESSURE-SINKAGE TEST

The first step for a semi-empirical method is to estimate the stress distribution (both normal and shear stresses) developed at the interface between a plate and the soil surface as a result it helps in predicting the load bearing property of the soil. The normal stress is calculated from the pressure-sinkage equation originally introduced by Bekker [4] and later modified by Reece (3.1),

$$p = \left(ck_c^{'} + \gamma_s bk_\varphi^{'}\right)(z/b)^n \tag{41}$$

where,

p = pressure normal to the sinkage plate

z = sinkage

n = sinkage index

c = soil cohesion

γ = soil density

$\overset{k'}{c}$ = cohesion dependent soil coefficient

$\overset{k'}{\varphi}$ = frictional dependent soil coefficient

b = parameter related to the geometry of the penetrometer (the smaller linear dimension for rectangular plates)

The equation is a modified version of the Bekker sinkage-pressure equation (2.2), also known as Bekker-Reece equation, where the ratio z/b is introduced for two reasons: make the parameters k_c and k_φ dimensionless and provide a single equation that accounts for different plate shapes. The exponent n, is crucial because it defines the trend of the relationship. Most soils behave almost linearly having n in the range of 0.8 to 1.2. The density γ can be readily obtained while the cohesion c is usually calculated through a series of uni-axial and tri-axial compression tests. The sinkage index n, and the constants k_c and k_φ are obtained using a bevameter or a penetrometer. These devices apply a constantly increasing load on a plate which is pushed perpendicularly down into the terrain. At the same time the sinkage is measured and the experimental data points are assumed to be represented by sinkage z and normal pressure σn are recorded. The experimental data is then fitted with (3.1).

4.1 Experiment and Simulation

Pressure-sinkage experiment as mentioned above is performed to seek soils capability to react with normal pressure when a plate pushed into it at a constant velocity. As a result it is important to tune the DEM soil model in the Multibody Dynamics tool to get close co-relation between the test and simulation to emulate an accurate model of the soil specimen.

The test rig [37] consists of a pressure plate which is connected to a force sensor that senses normal force applied on the pressure plate surface. The whole setup is connected to a linear actuator which pushes the pressure plate into a soil specimen bath. In the simulation we remained careful selecting the soil bath size to avoid edge affects causing soil hardening. Also, depth of the soil so selected that it has enough clearance below the soil even after full travel of the actuator. In the simulation before the pressure plate is activated we get the soil top surface smoothened to avoid disturbances in the force sensor data.

In the experimental setup the pressure plates are made of Aluminum, therefore minimizing friction between plate and sand. The constant velocity at which the pressure plate is pushed down is 10mm/s. There is little disturbances in the velocity during the experiment but it is assumed negligible in simulation and constant velocity is provided to the pressure plate by the linear actuator.

In the experiment, various widths of pressure plates hae been used to accurately understand the variation of normal pressure with change in the contact area. Similarly, we have captured the same in simulation and tried to achieve similar results.

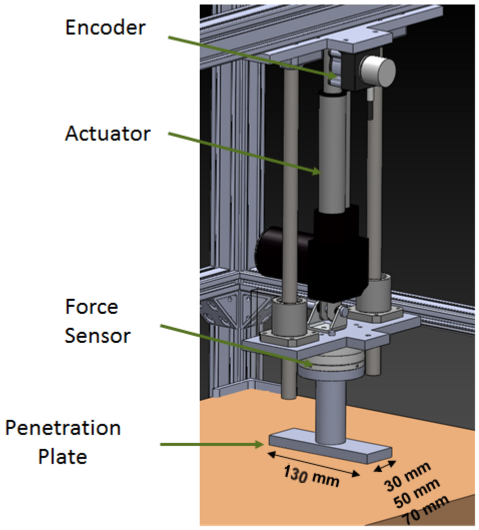

Fig. 4.1. Pressure sinkage penetroplate experimental setup [36]

Table 4.1.
MBD model properties for pressure-sinkage penetroplate simulation

Number of rigid bodies	5
Number of prismatic joints	4
Number of linear actuator	4

4.2 Results and Explanation

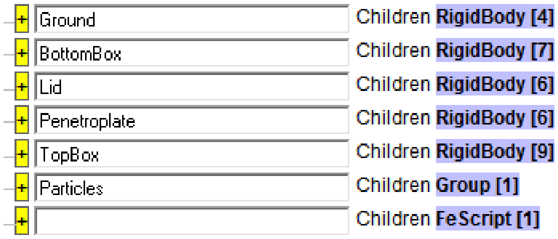

+ Ground Children RigidBody [4]
+ BottomBox Children RigidBody [7]
+ Lid Children RigidBody [6]
+ Penetroplate Children RigidBody [6]
+ TopBox Children RigidBody [9]
+ Particles Children Group [1]
+ Children FeScript [1]

Fig. 4.2. MBD simulation model hierarchy

The multibody dynamics model of the pressure-sinkage experiment with penetroplate consist of the ground, bottom box, penetroplate, top box and DEM particles as in Figure 4.2 and Table 4. Similar to the direct shear stress experiment the particle box is dropped into the box space of 0.25m x 0.20m x 0.44m at a three dimensional angle. The box space is so selected to reduce the computational time yet avoid edge affect on the simulation results. Then the lid gets activated throught the linear actuator and drops to the particle surface and make the top surface even. Similarly the penetroplate gets activated falls on the particle surface from there on it follows a steady speed of 10 mm/s and the normal force to the penetroplate bottom surface exerted by the particles is recorded by the force sensor. The simulation similar to the experiment is repeated with 3 different penetroplate sizes that is 130mm x 30mm x 10mm; 130mm x 50mm x 10mm; and 130mm x 70mm x 10mm. A total number of particles used 209664 with particle radius of 0.00186m (Figure 4.5).

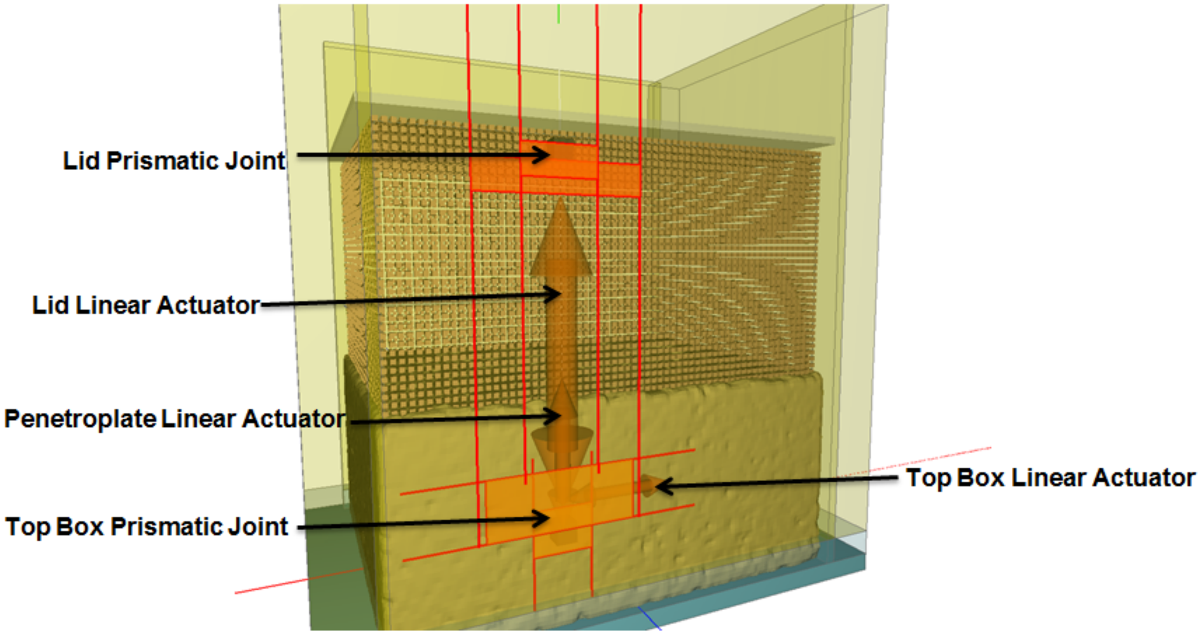

Fig. 4.3. Joints and actuators in the MBD model of penetroplate pressure sinkage test

Table 4.2.
Particle properties for pressure-sinkage penetroplate simulation

Number of particles	209664
Particle radius (m)	0.00186
Particle shape	Cuibcal-8 glued spheres
Normal contact stiffness (N)	2000
Normal contact damping (N.sec)	0.015
Separation damping factor	0.05
Coefficient of friction	0.4

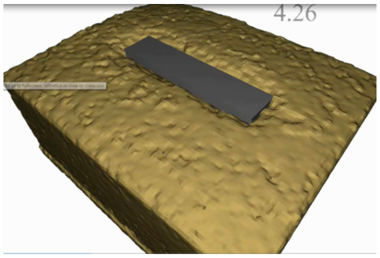

Fig. 4.4. Snapshot of penetroplate pressure sinkage simulation

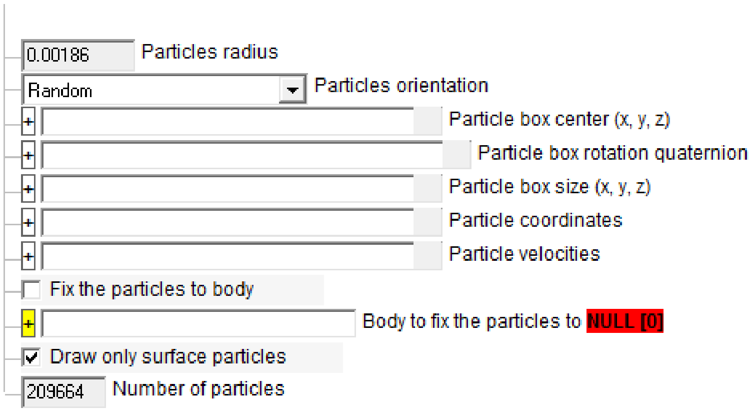

0.00186 Particles radius

Random Particles orientation

+ Particle box center (x, y, z)

+ Particle box rotation quaternion

+ Particle box size (x, y, z)

+ Particle coordinates

+ Particle velocities

☐ Fix the particles to body

+ Body to fix the particles to NULL [0]

☑ Draw only surface particles

209664 Number of particles

Fig. 4.5. DEM particle model inside IVRESS showing number of particles and particle radius

As it can be seen from Figure 4.6 and Table 5 the particle-particle contact properties are identical to the direct shear stress simulation therefore it is the same DEM soil model except the contact tolerance and search tolerance had to be adjusted due to change in the particle radius.

It can be seen from Figure 4.9 that the change in pressure on the plate surface relative to the sinkage has the same trend as that of the experiment but there is a small offset in case of Figure 4.10. This may have been caused by edge effect, randomization of the particles and error while digitization and averaging the experimental data. In the case of Figure 4.11, there is a discrepancy regarding the experimental results as the pressure for 70mm plate should have been more than 30mm and 50mm plates but

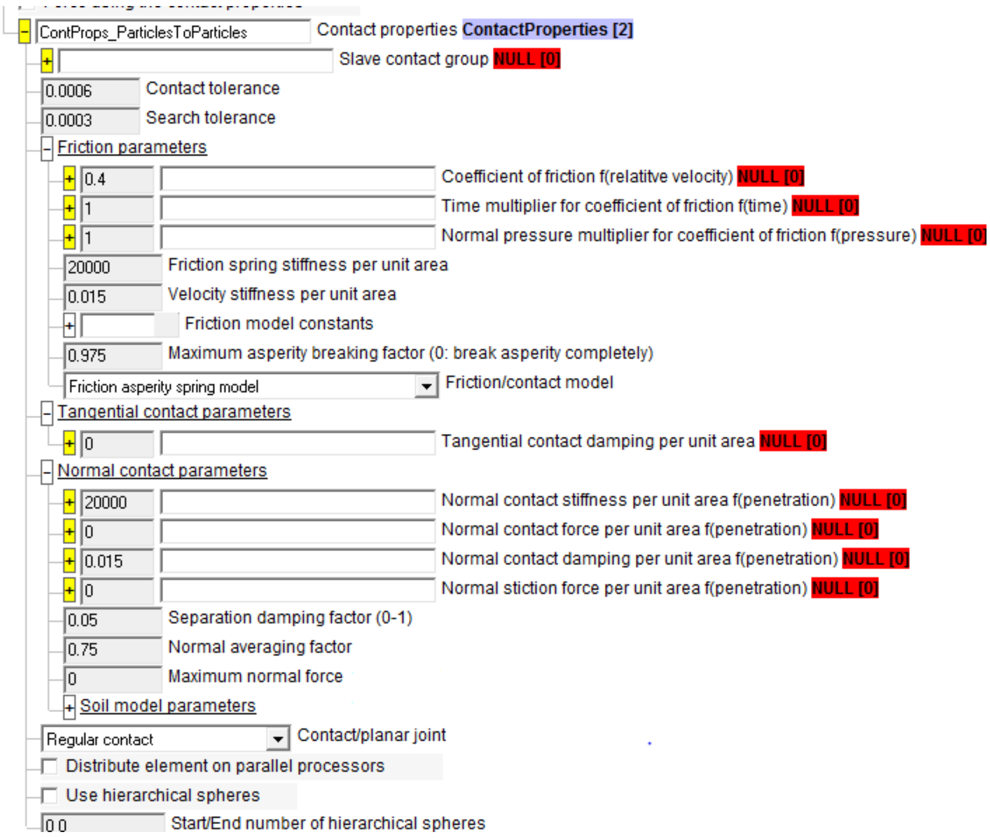

ContProps_ParticlesToParticles Contact properties ContactProperties [2]

Slave contact group NULL [0]

0.0006 Contact tolerance

0.0003 Search tolerance

Friction parameters

0.4 Coefficient of friction f(relative velocity) NULL [0]

1 Time multiplier for coefficient of friction f(time) NULL [0]

1 Normal pressure multiplier for coefficient of friction f(pressure) NULL [0]

20000 Friction spring stiffness per unit area

0.015 Velocity stiffness per unit area

Friction model constants

0.975 Maximum asperity breaking factor (0: break asperity completely)

Friction asperity spring model Friction/contact model

Tangential contact parameters

0 Tangential contact damping per unit area NULL [0]

Normal contact parameters

20000 Normal contact stiffness per unit area f(penetration) NULL [0]

0 Normal contact force per unit area f(penetration) NULL [0]

0.015 Normal contact damping per unit area f(penetration) NULL [0]

0 Normal stiction force per unit area f(penetration) NULL [0]

0.05 Separation damping factor (0-1)

0.75 Normal averaging factor

0 Maximum normal force

Soil model parameters

Regular contact Contact/planar joint

☐ Distribute element on parallel processors

☐ Use hierarchical spheres

0 0 Start/End number of hierarchical spheres

Fig. 4.6. IVRESS snapshot showing particle-particle contact properties

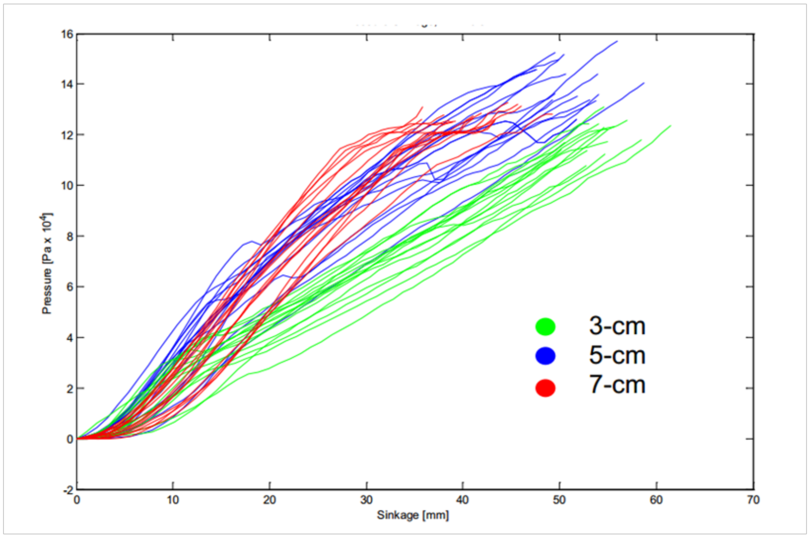

Fig. 4.7. Experimental results showing pressure vs sinkage at different plate widths [37]

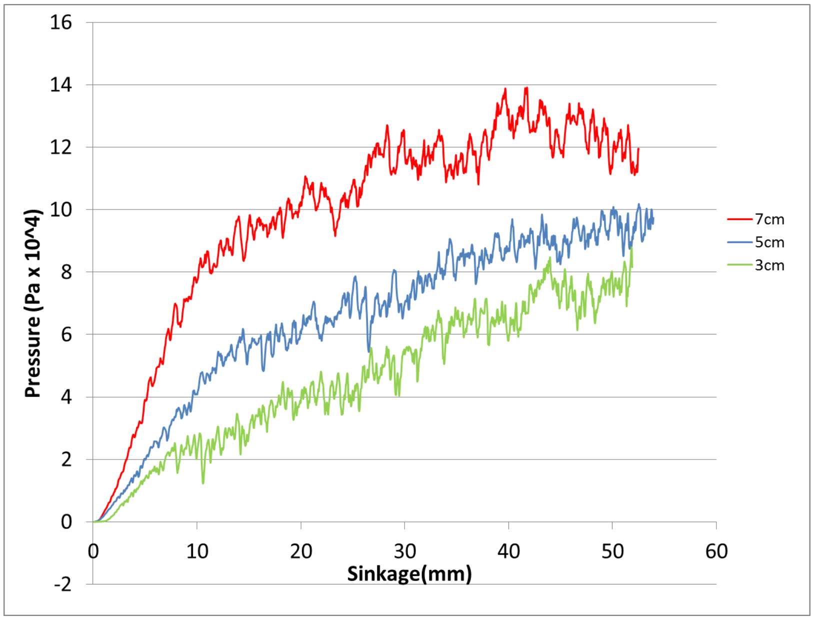

Fig. 4.8. Simulation results showing pressure vs sinkage at different plate widths

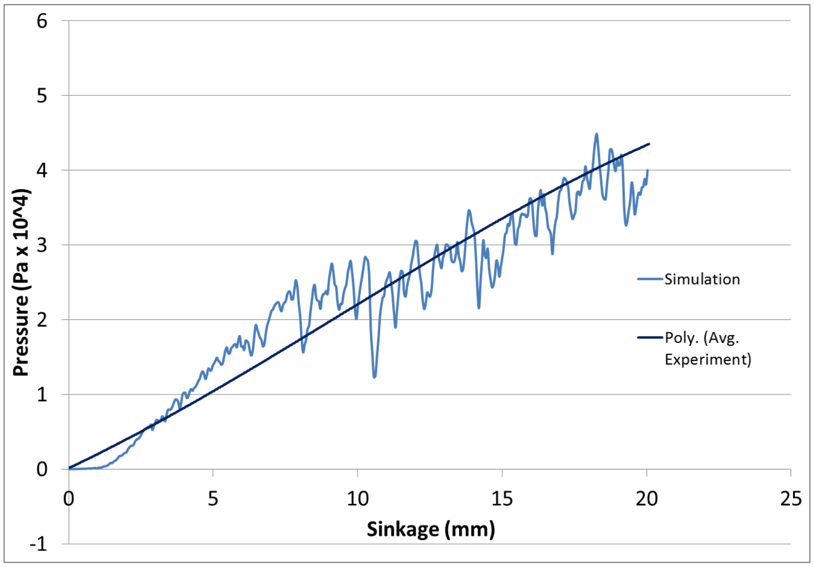

Fig. 4.9. Comparison between simulation results and experimental results poly-fitted at 3cm plate width

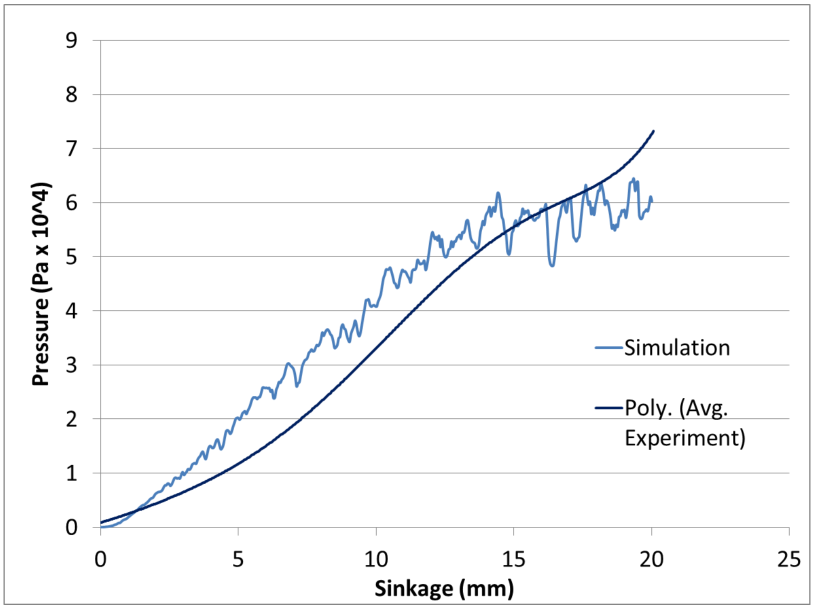

Fig. 4.10. Comparison between simulation results and experimental results poly-fitted at 5cm plate width

it dipped down. Therefore the experimental results are probably not accurate for the 70 mm plate

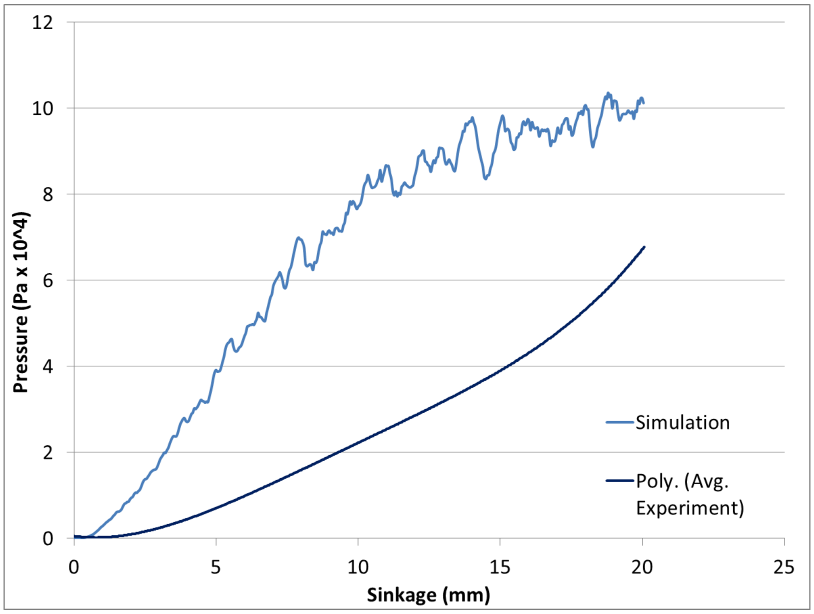

Fig. 4.11. Comparison between simulation results and experimental results poly-fitted at 7cm plate width

5. RIGID WHEEL-SOIL INTERACTION

The main reasons to study vehicle-terrain interaction in the course of this research are to validate and predict using an actual mobility application on the DEM soil model tuned and calibrated in the previous experiments. This will lead us to predict the performance of an off-road vehicle using parameters which have been obtained in this experiment at different slip percentage like draw-bar pull force, tractive efficiency, sinkage of the tire into the soft soil. These parameters will help the designer to predict most suitable vehicle system on soft soil like brake controls, suspension, tires and anticipate performance outcomes.

Slip Percentage:

Slip is relative motion between the soil and the vehicle, and it can be calculated by finding the difference between the linear velocity of the vehicle and the linear speed calculated from the angular velocity of the wheels.

$$slip = \frac{\omega r - v}{v} \tag{42}$$

Sinkage:

Sinkage at wheel-soil interface is the measurement of the vertical displacement of the wheel while it is operating on the soft soil caused due to compaction and shearing of the soil surface.

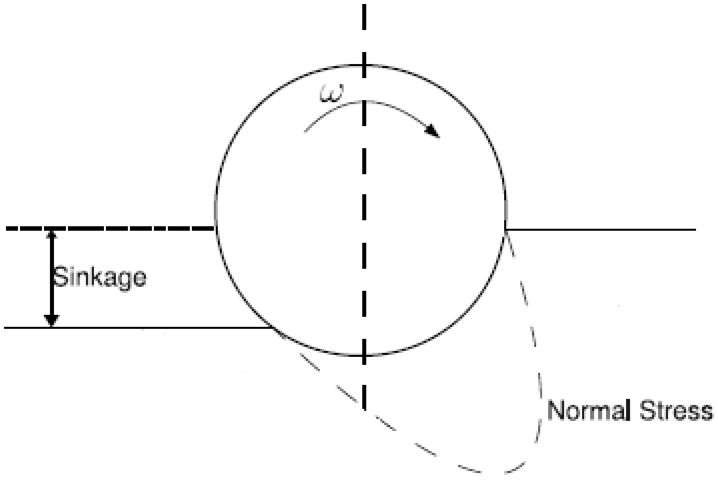

Fig. 5.1. Sinkage of a wheel on soft soil

Drawbar Pull Force:

Drawbar pull force is the net force available at a vehicle's hitch, which is under steady state condition is the difference between thrust given to the vehicle and resistive forces [1].

$$F_d = F - \sum R \tag{43}$$

Tractive Efficiency:

The resistance in motion at the tire-soil interface is caused due to sinkage. Tractive efficiency is a measure of the capability of converting power into effective mobility which depends on wheel radius and slip ratio [1].

$$\eta_t = \frac{F_x v_x}{T\omega} = \frac{F_x \left(1 - s_d\right) R_t}{T} \tag{44}$$

5.1 Experimental Setup

A tire working on a soft soil can be assumed rigid wheel unless the pressure distribution at the contact patch is more than the carcass stiffness. Therefore, we emulated the test performed previously in our simulation. The test and simulation setup consist of a big soil bath with considerable dimensions compared to the wheel dimensions to avoid edge effects. The wheel carries a carriage which is attached to a linear actuator giving a constant linear speed to the wheel. The wheel runs on a rotational actuator, therefore, varying the carriage speed and the wheel speed one can obtain any slip percentage. In the simulation sinkage of the wheel into the soil is measured by measuring the displacement of the carriage actuator.

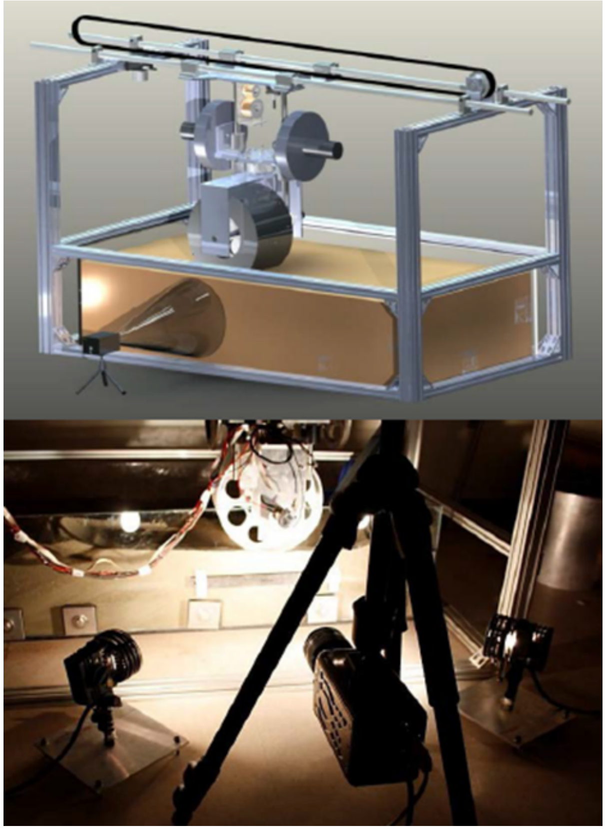

Fig. 5.2. Experimental setup of the wheel test experiment [37]

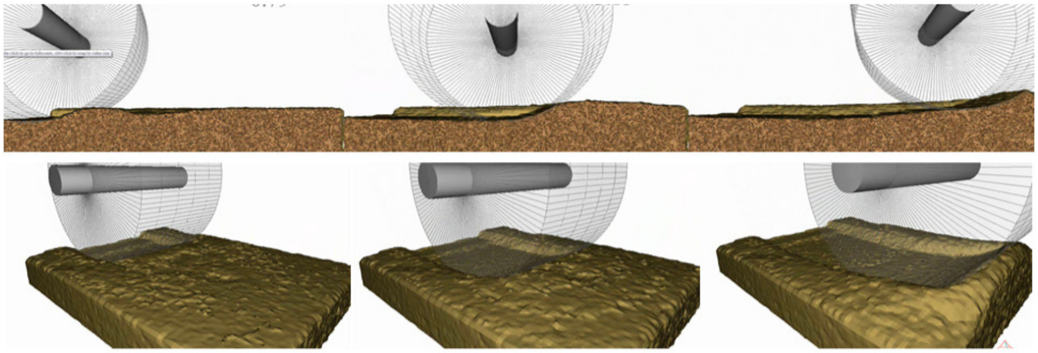

Fig. 5.3. Snapshots of the wheel test simulation from two different angles

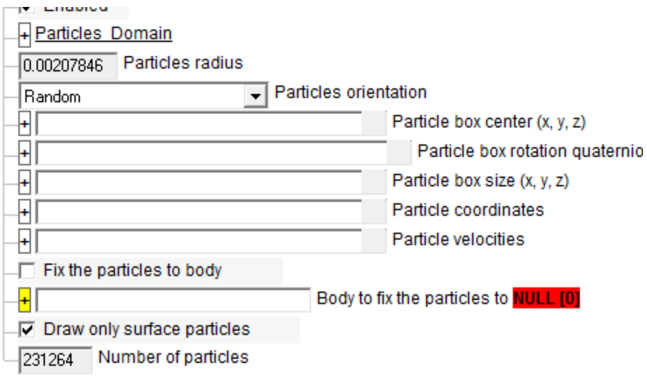

Particles_Domain

0.00207846 Particles radius

Random Particles orientation

Particle box center (x, y, z)

Particle box rotation quaternio

Particle box size (x, y, z)

Particle coordinates

Particle velocities

☐ Fix the particles to body

Body to fix the particles to NULL [0]

☑ Draw only surface particles

231264 Number of particles

Fig. 5.4. DEM particle model inside IVRESS showing number of particles and particle radius

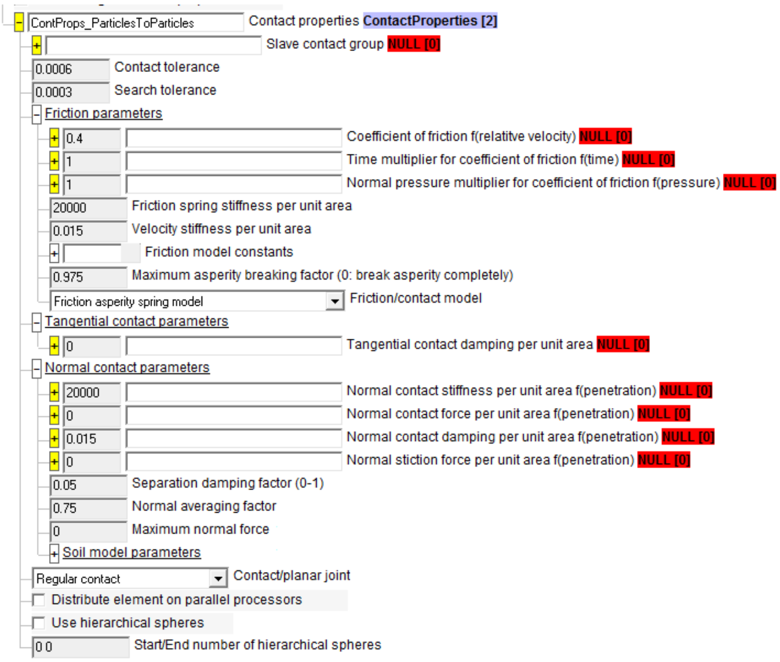

ContProps_ParticlesToParticles Contact properties ContactProperties [2]

Slave contact group NULL [0]

0.0006 Contact tolerance

0.0003 Search tolerance

Friction parameters

0.4 Coefficient of friction f(relative velocity) NULL [0]

1 Time multiplier for coefficient of friction f(time) NULL [0]

1 Normal pressure multiplier for coefficient of friction f(pressure) NULL [0]

20000 Friction spring stiffness per unit area

0.015 Velocity stiffness per unit area

Friction model constants

0.975 Maximum asperity breaking factor (0: break asperity completely)

Friction asperity spring model Friction/contact model

Tangential contact parameters

0 Tangential contact damping per unit area NULL [0]

Normal contact parameters

20000 Normal contact stiffness per unit area f(penetration) NULL [0]

0 Normal contact force per unit area f(penetration) NULL [0]

0.015 Normal contact damping per unit area f(penetration) NULL [0]

0 Normal stiction force per unit area f(penetration) NULL [0]

0.05 Separation damping factor (0-1)

0.75 Normal averaging factor

0 Maximum normal force

Soil model parameters

Regular contact Contact/planar joint

☐ Distribute element on parallel processors

☐ Use hierarchical spheres

0 0 Start/End number of hierarchical spheres

Fig. 5.5. IVRESS snapshot showing particle-particle contact properties

Table 5.1.
Particle properties for rigid wheel test simulation

Number of the particles	231264
Radius of particles	0.00207846
Normal contact stiffness (N-m)	2000
Normal contact damping (N-sec/m)	0.015
Separation damping factor	0.05
Coefficient of friction	0.4

5.2 Results and Explanation

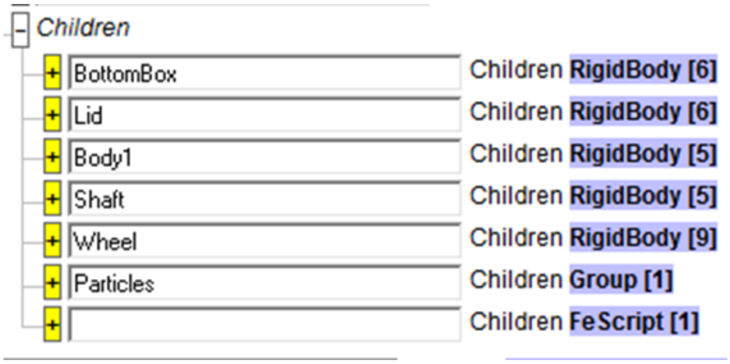

Children

BottomBox	Children **RigidBody [6]**
Lid	Children **RigidBody [6]**
Body1	Children **RigidBody [5]**
Shaft	Children **RigidBody [5]**
Wheel	Children **RigidBody [9]**
Particles	Children **Group [1]**
	Children **FeScript [1]**

Fig. 5.6. MBD simulation model hierarchy

Table 5.2.
MBD model properties

Number of rigid bodies	5
Number of prismatic joints	3
Number of revolute joints	1
Number of linear actuator	2
Number of rotary actuator	1

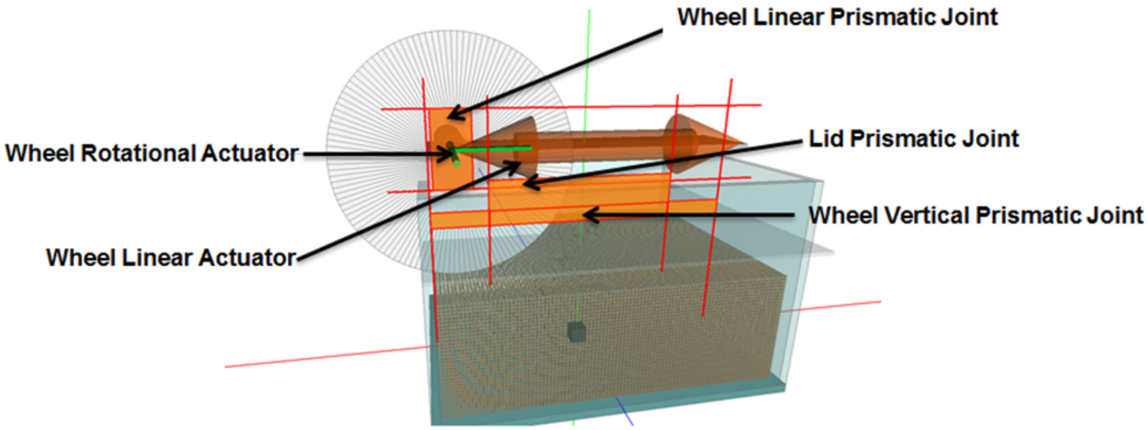

Fig. 5.7. Joints and actuators in the MBD model of wheel test

The multibody dynamics model consists of a bottom box, lid, body, shaft, wheel and the DEM particles. The soil bath used in the experiment has a dimension of 0.4m x 0.3m x 0.5m considering the length the wheel will take to reach a steady state speed and enough room is available to collect data without edge affect affecting the data, yet trying to keep the computational time minimum. A lid actuator is used to normalize the top surface of the soil. The total number of soil particles used is 231264 with particle radius 0.002078 m with identical contact properties as that of the penetroplate experiment as seen from the Figure 5.4. As shown in Figure 5.7 there is two actuator one is the linear actuator giving a linear speed to the body and a rotational actuator rotating the shaft. The difference in speed being created by the two actuators creates the slip percentage. For this experiment the wheel speed is kept constant and slip percentage is varied by changing the body speed. Table 2 represents different body speed at different slip percentage. Data has been recorded when the system reached a steady state and is near the center of the tank to avoid edge effects.

It is visually evident from Figure 5.8 that the DEM soil model has the most resemblance to the experimental wheel torque trend at different slip percentage. The

Table 5.3.
Body speed at different slip

Slip%	Wheel Speed(deg/s)	Wheel Speed(rad/s)	Wheel Speed(m/s)	Body Speed(m/s)
-70.00%	17	0.296705973	0.038571776	0.06557202
-50.00%	17	0.296705973	0.038571776	0.057857665
-30.00%	17	0.296705973	0.038571776	0.050143309
-10.00%	17	0.296705973	0.038571776	0.042428954
0.00%	17	0.296705973	0.038571776	0.038571776
10.00%	17	0.296705973	0.038571776	0.034714599
30.00%	17	0.296705973	0.038571776	0.027000244
50.00%	17	0.296705973	0.038571776	0.019285888
70.00%	17	0.296705973	0.038571776	0.011571533

empirical model have great offsets as it is not physically possible to tune them to match experimental results.

Similarly, in the case of drawbar force the overall trend followed byt the DEM soil model in this paper resembles greatly with the experimental results. The error is on higher side near 0% slip and 10% slip which can be seen in Figure 5.9.

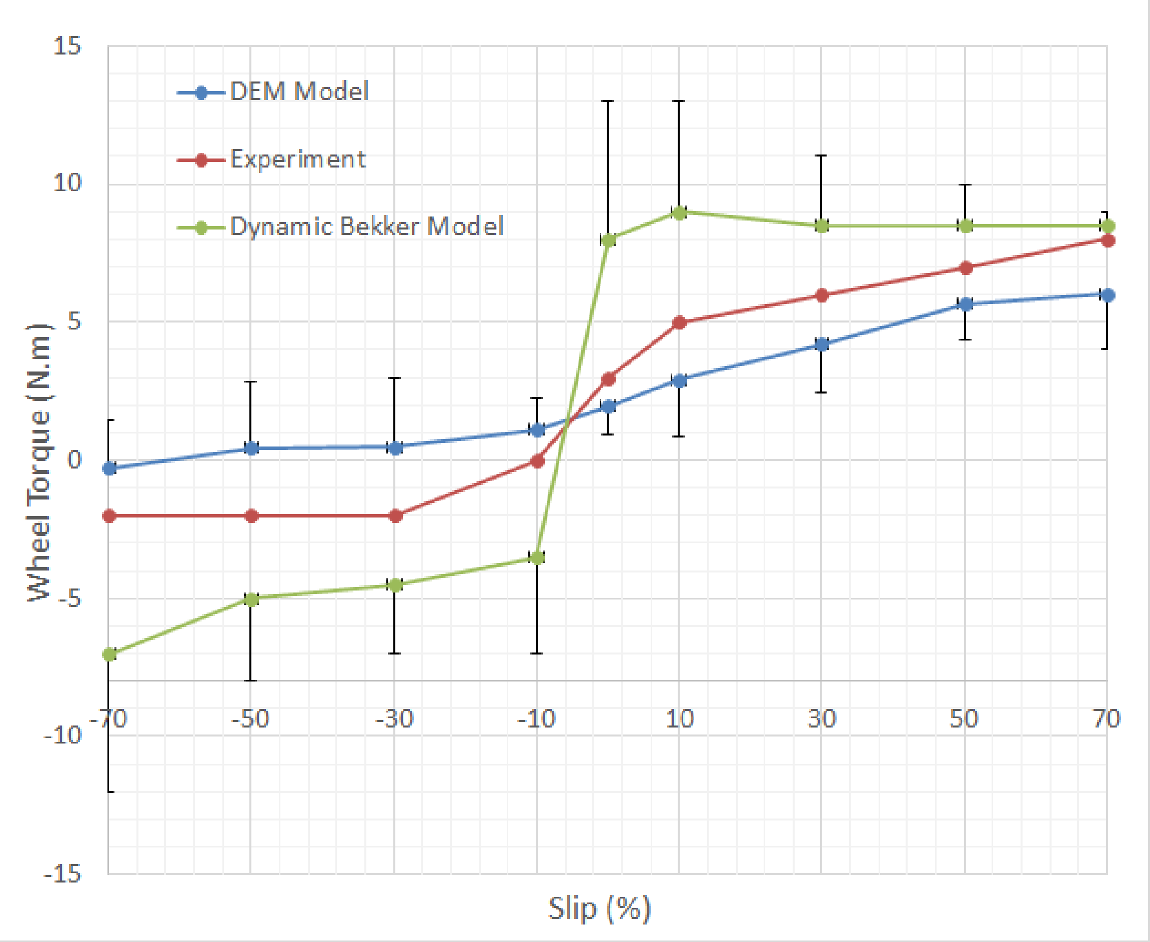

Fig. 5.8. Comparison of wheel torque - slip % between different terramechanics approaches with bars showing error compared to the experimental results [10]

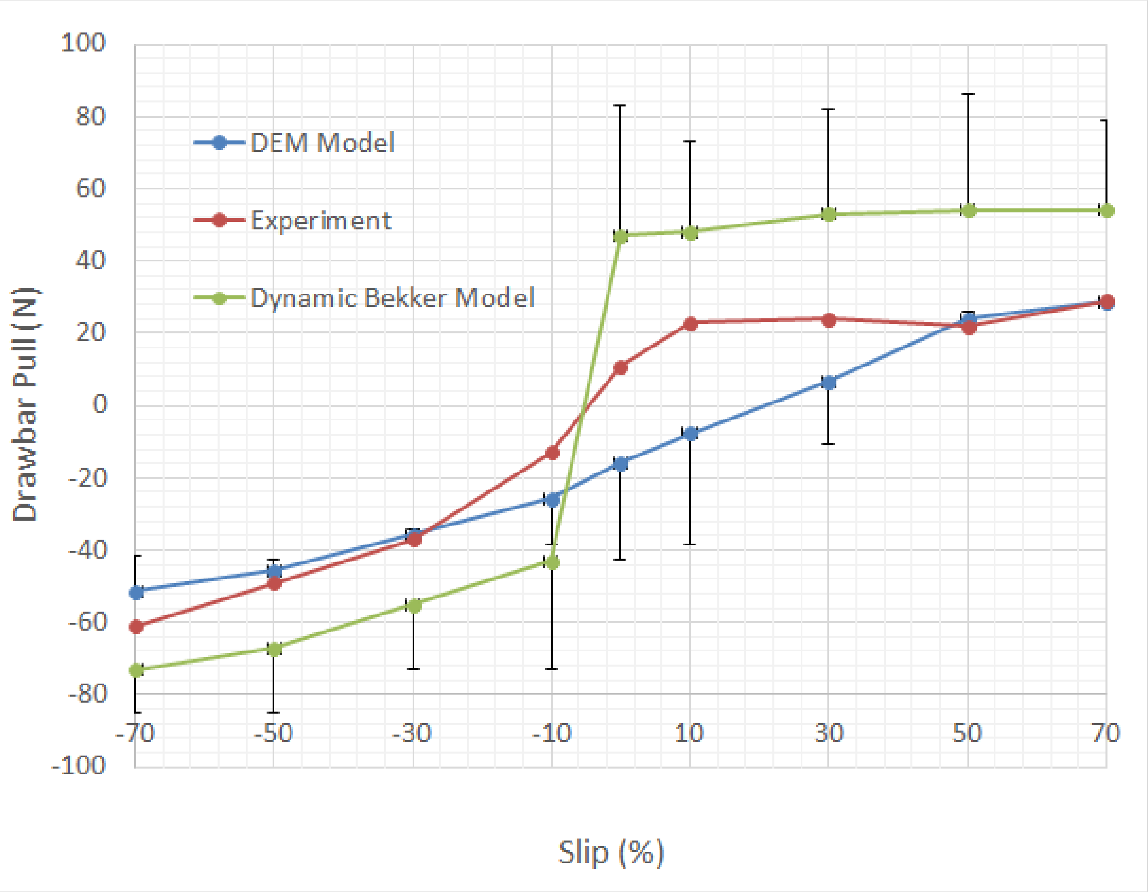

Fig. 5.9. Comparison of drawbar force - slip % between different terramechanics approaches with bars showing error compared to the experimental results [10]

6. APPLICATION: PREDICTION OF MOBILITY OF A HUMVEE VEHICLE ON SOFT SOIL

In this section, we present a simulation of a Humvee-type vehicle driving on a soft soil terrain with varying soil types, long slopes and side slopes. A parallel explicit solution procedure is used to solve equations of motion along with the constraint and is implemented in the DIS software code. The DIS code was used to create the coupled multibody dynamics model of the vehicle and DEM soil model and to generate the simulation results. Figures 6.1 and Figure 6.2 shows the vehicle multibody dynamics model. As stated in Table 10, the MBD model consists of 34 rigid bodies: main chassis; 4 wheels; 4 upper suspension control arms; 4 lower suspension control arms; 4 knuckles; 6 bodies for the front axle; 6 bodies for the rear axle; drive shaft; 2 tie rods; steering pinion; and steering rack. The bodies are connected using spherical, revolute, prismatic and CV joints. A rotational actuator at the drive shaft is used to model the engine and four rotational actuators at the wheels are used for modeling the brakes. The total sprung mass of the vehicle is 4,430 kg. The mass of one wheel is 50 kg. Each tire polygonal surface consists of 6662 triangles [38] (Figure 6.3). The tire diameter is 0.97 m. The tires' surfaces are set as slave contact surfaces for the DEM particles. As stated in Table 9 the DEM particle contact properties are identical to previously described simulations. The total number of particles used for this simulation is 331890 with radius of 0.023m.

Spherical joints are used to model the following front suspension joints [38]:

- Two ball joints between the suspension control arms and the steering knuckle in the front suspension system.
- Ball joint between the steering rack and the tie rod.
- Ball joint between the steering knuckle and the tie rod.

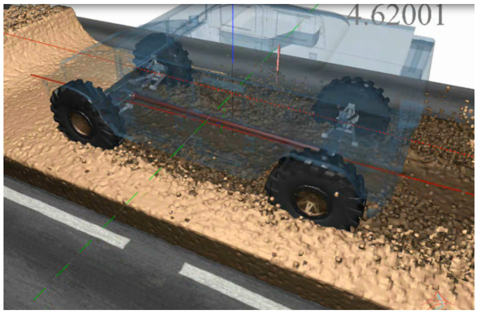

Fig. 6.1. Humvee MBD simulation on soft soil [38]

Table 6.1.
Particle properties for full vehicle simulation

Number of the particles	331890
Radius of particles	0.023
Normal contact stiffness (N-m)	2000
Normal contact damping (N-sec/m)	0.015
Separation damping factor	0.05
Coefficient of friction	0.4

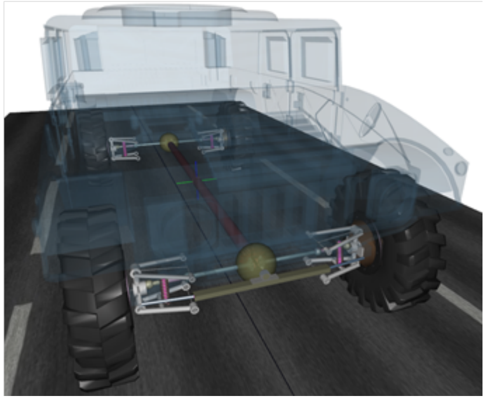

Fig. 6.2. Humvee MBD model [38]

The stiffness and damping of the joint are set equal to the radial stiffness and damping of the ball joints bushings.

Table 6.2.
MBD model properties of the vehicle

Number of rigid bodies	34
Number of prismatic joints	3
Number of revolute joints	16
Number of spherical joints	6
Bumber of CV joint	4
Number of rotary actuator	5

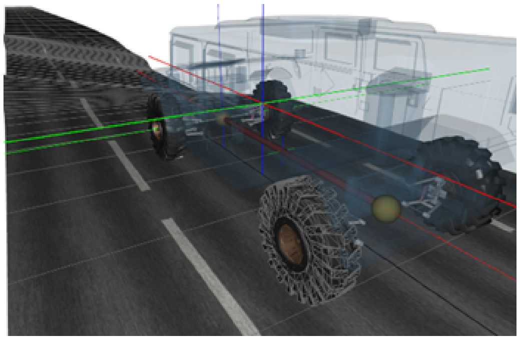

Fig. 6.3. Polygon surface of the tire [38]

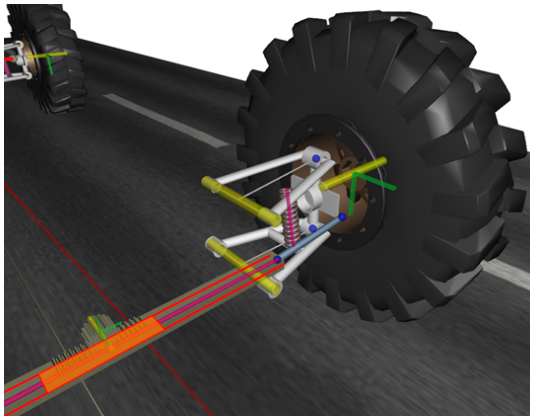

Fig. 6.4. Various suspension joints of the vehicle [38]

Revolute joints are used to model most of the vehicle joints including [38]:

- Joints between the suspension control arms, knuckle, and frame.
- Joint between the wheel and knuckle.
- Joints between the axle and the frame.
- Joint between the drive shaft and the frame.

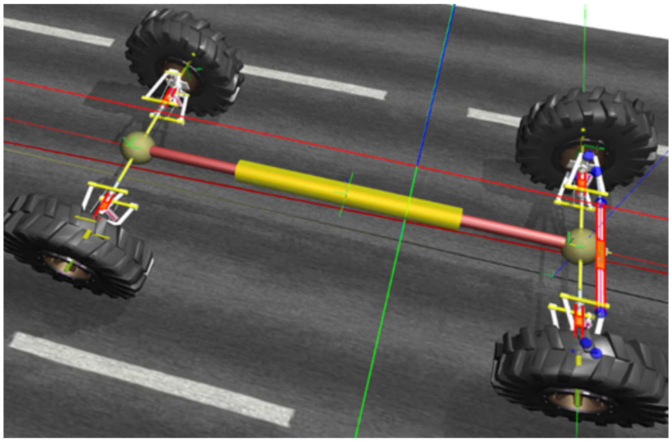

Fig. 6.5. MBD model of the entire vehicle chassis system [38]

7. CONCLUDING REMARKS AND FUTURE WORK

An explicit time integration multibody dynamics code was used to create a three-dimensional multibody dynamics model of 3 experiments and a full vehicle simulation, in order to calibrate a DEM soil model. The model has the following major characteristics:

- A high fidelity multibody dynamics models are used for the experiments and the full vehicle simulations.
- Particles geometric shape can be modeled using three types of shape representations: superquadric surface, assembly of spheres, and polygonal surface.
- A Cartesian Eulerian grid contact search algorithm is used to allow fast contact detection between particles.
- Normal contact constraints are modeled using the penalty technique with a penalty spring and an asymmetric damper.
- Friction is modeled using an asperity-based approximate Coulomb friction model.
- The rigid bodies rotational equations of motion are written in a body-fixed frame with the total rigid body rotation matrix updated each time step using incremental rotations.
- The governing equations of motion are solved along with the contact constraint equations using a time-accurate explicit solution procedure.

The soil model was used to validate experimental using cubical sand particles Parametric studies were performed in order to study the effects of the particle size and contact properties on the simulation results. The simulation results found to be in very good co-relation with the experimental result.

Recommended Future Work

- Future work to be done to improve the correlation between experimental results and simulation results by using a definite algorithm to tune contact properties.
- There is a necessity to perform further more soil experiments and validate the DEM model using the experimental results to improve soil model fidelity by increasing soil target properties like compressibility, bulk density, slope stability, particle size.
- The edge effect of the soil particle container played a significant role in this research and required many iterations to avoid such affects therefore work needs to be done to identify correct sizing of the soil container which will eliminate multiple iterations.
- Also, it is important to include cohesiveness of the soil and mixing multiple soils in the simulation to represent accurately a real life heterogeneous soil.
- It is important to introduce flexible and pneumatic tires on the soft soil and perform simulations to identify and caliberate tire parameters (tire pressure, tread shapes etc.) to make it more efficient for vehicle application.
- Work needs to be done to validate full vehicle simulation results with proving grounds results of a vehicle on a similar kind of soil.

REFERENCES

REFERENCES

[1] Wong, J. (2010). Terramechanics and Off-road Vehicle Engineering. Butterworth-Heinemann.

[2] Knight, S. (1961). "Measuring Soil Trafficability Characteristics,". National Technical Information Service.

[3] Bekker, M. (1964). "Mechanics of locomotion and lunar surface vehicle concepts,".SAE Transactions.

[4] Bekker, M. (1960). "Off-the-road locomotion,". The University of Michigan Press, Ann Arbor, Michigan.

[5] Bekker, M. (1956). "Theory of land locomotion,". The University of Michigan Press, Ann Arbor, Michigan.

[6] Reece and Wong J. (1967). "Prediction of rigid wheel performance based on the analysis of soil-wheel stresses part I. Performance of driven rigid wheels,". J. Terramechanics, vol. 4, p. 81–98.

[7] Reece and Wong J. (1967). "Prediction of rigid wheel performance based on the analysis of soil-wheel stresses part II. Performance of towed rigid wheels,". J. Terramechanics, vol. 4, pp. 7-25.

[8] Fattah, R. N. Y. and E. A. (1976). "Prediction of wheel-soil interaction and performance using the finite element method,". J. Terramechanics, vol. 13, no. 4, p. 227–240.

[9] Knuth, M. A., Johnson, J.B., Hopkins, M. A., Sullivan, R. J. and Moore, J. M. (2011). "Discrete element modeling of a Mars Exploration Rover wheel in granular material,". J. Terramechanics.

[10] Smith, W., Melanz, D., Senatore, C., Iagnemma, K. and Peng, H. (2013) "Comparison of DEM and traditional modeling methods for simulating steady-state wheel-terrain interaction for small vehicles".

[11] Wong, C. and L. J.Y. (1996). "Numerical simulations of tire-soil interaction based on critical state soil mechanics,". Journal of Terramechanics, vol. 33(5), pp. 209-221.

[12] Karafiath, L. (1984). "Finite element analysis of ground deformation beneath moving track loads," . 8th International Conference of International society for Terrain-Vehicle Systems.

[13] Tsuji, T., Nakagawa, Y., Matsumoto, N., Kadono, Y., Takayama, T. and Tanaka, T. (2012). "3-D DEM simulation of cohesive soil-pushing behavior by bulldozer blade,". J. Terramechanics, vol. 49, p. 37–47.

[14] Cundall, P. (1971) "A computer model for simulating progressive large-scale movements in block rock mechanics,". Proc. Symp. Int. Soc. Rock Mech. Nancy, vol. 2.

[15] Cundall, P. and Strack, O. (1979). "A discrete numerical model for granular assemblies,". Geotechnique, vol. 29, no. 1, pp. 47-65.

[16] Horner, D., Peters, J. and Carrillo, A. (1979). "Large Scale Discrete Element Modeling of Vehicle-Soil Interaction,". Journal of Engineering Mechanics, vol. 127, pp. 1027-1032.

[17] Carrillo, A., Horner, D., Peters, J., and West, J. (1996). "Design of a Large Scale Discrete Element Soil Model for High Performance Computing Systems,". ACM/IEEE conference on Supercomputing.

[18] Drucker, D. C. and Prager, W. (1952). "Soil mechanics and plastic analysis for limit design,". Quarterly of Applied Mathematics, vol. 10, no. 2, pp. 157-165.

[19] Youngs, D. (1987). "An interface tracking method for a 3D Eulerian hydrodynamics code,". Technical Report Atomic Weapons Research Establishment.

[20] Hirt, C. and Nichols, B. (1981). "Volume of fluid (VOF) method for the dynamics of free boundaries,". Journal of Computational Physics, vol. 39, pp. 201-225.

[21] Wasfy, T., O'Kins, J. and Smith, S. (2008). "Experimental Validation of a Time-Accurate Finite Element Model forCoupled Multibody Dynamics and Liquid Sloshing,". SAE 2007 Transactions, Journal of Passenger Cars: Mechanical Systems, Vols. 2007-01-0139.

[22] Wasfy, T.M. (2004). "Modeling spatial rigid multibody systems using an explicit-time,". 28th Biennial Mechanisms and Robotics Conference, Salt Lake, Utah.

[23] Wasfy, T. (2003). "Asperity spring friction model with application to belt-drives,". DETC2003.

[24] Coetzee, C.J., Basson, A.H. and Vermeer, P. A. (2007). "Discrete and continuum modeling,". Journal of Terramechanics, vol. 44, pp. 177-186.

[25] Elperin, T. and Golshtein, E. (1997). "Comparison of di," Physica A, vol. 242, pp. 332-340.

[26] Advanced Science and Automation Corp. "DIS :Dynamic Interactions Simulator,". Retreived from http://www.ascience.com. [Accessed March 2013].

[27] Leamy, M. J. and Wasfy, T.M. (2002). "Transient and steady-state dynamic,", vol. 124, no. 4, pp. 575-581.

[28] Wasfy, T. (2015). "Introduction to Hybrid-Electric Vehicle,". IUPUI Course ME 5970.

[29] Cundall, P.A. (1988). "Formulation of a three-dimensional distinct element model Part,". International Journal of Rock Mechanics, Mining Science, vol. 25, no. 3, pp. 107-116.

[30] Ahmadi, S. G., Wasfy, T. M., Wasfy, H. M., and Peters, J. M. (2013). "High-Fidelity modeling of a backhoe digging operation using an explicit multibody dynamics code with integrating discrete particle modeling capability,". Published by ASME.

[31] Wasfy, T. M., Ahmadi, S. G., Wasfy, H. M. and Peters, J. M. (2013) "Multibody Dynamic Modeling of Sand Flow from Hopper and Sand Pile Angle of Repose,". ASME International Design Engineering Technical Conference.

[32] Wang, J. and Gutierrez, M. (2010). "Discrete element simulations of direct shear specimen scale effects".

[33] Janosi, Z. and Hanamoto, B. (1961). "The analytical determination of drawbar pull as a function of slip for tracked vehicles in deformable soils,". 1st International Conference on the Mechanics of Soil-Vehicle Systems, Torino, Italy.

[34] Janosi, Z. (1961). "An analysis of pneumatic tire performance on deformable soil,". 1st International Conference on the Mechanics of Soil-Vehicle Systems, Troino, Italy.

[35] Melanza, D., Jayakumara P. and Negrut, D. (2015). "Experimental Validation of a Differential Variational Inequality-Based Approach," US Army RDECOM-TARDEC, Warren, Michigan.

[36] Senatore, C. (2014). "Robotic Mobility Group; Laboratory for Manufacturing and Productivity; MIT,". Cambridge, MA.

[37] Senatore, C., Wulfmeier, M., MacLennan, J., Jayakumar, P. and Iagnemma, K. (2012). "Investigation of stress and failure in granular soils for lightweight robotic vehicle application,". NDIA Ground Vehicle Systems Engineering and Technology Symposium, Michigan.

[38] Wasfy, T. M., Wasfy, H. M. and Peters, J. M. (2015). "High-Fidelity Multibody Dynamics Vehicle Model Coupled with Cohesive Soil Discrete Element Model for predicting Vehicle Mobility,". ASME International Design Engineering Technical Conference; 11th International Conference on Multibody Systems, Nonlinear Dynamics, and Control (MSNDC), Boston, MA, USA.

[39] Regli, G., Handke A. and Bütikofer (1993). "Material laws as a basis for simulation models for the calculation of wheelsoil interaction examination using the finite element method,". Journal of Terramechanics, vol. 30, no. 3, pp. 165-179.

[40] Shoop, S., Richmond. P. and Lacombe, J. (2006). "Overview of cold regions mobility modeling at CRREL,". Journal of Terramechanics, vol. 43, no. 1, pp. 1-26.

[41] Tekestea, M., Tollnera, E., Raperb, R., Wayb, T. and Johnson, C. (2009). "Nonlinear finite element analysis of cone penetration in layered sandy loam soil - Considering precompression stress state,". Journal of Terramechanics, vol. 46, no. 5, pp. 229-239.

[42] Xia, K. (2011). "Finite element modeling of tire/terrain interaction: Application to predicting soil compaction and tire mobility,". Journal of Terramechanics, vol. 48, no. 2, pp. 113-123.